Deformation during the 1975–1984 Krafla rifting crisis, NE Iceland, measured from historical optical imagery

James Hollingsworth,[1] Sébastien Leprince,[1] François Ayoub,[1] and Jean-Philippe Avouac[1]

Received 9 January 2012; revised 16 September 2012; accepted 20 September 2012; published 14 November 2012.

[1] We measure the displacement field resulting from the 1975–1984 Krafla rifting crisis, NE Iceland, using optical image correlation. Images are processed using the COSI-Corr software package. Surface extension is accommodated on normal faults and fissures which bound the rift zone, in response to dike injection at depth. Correlation of declassified KH-9 spy and SPOT5 satellite images reveals extension between 1977–2002 (2.5 m average opening over 80 km), while correlation of aerial photos between 1957–1990 provide measurements of the total extension (average 4.3 m opening over 80 km). Our results show ~8 m of opening immediately north of Krafla caldera, decreasing to 3–4 m at the northern end of the rift. Correlation of aerial photos from 1957–1976 reveal a bi-modal pattern of opening along the rift during the early crisis, which may indicate either two different magma sources located at either end of the rift zone (a similar pattern of opening was observed in the 2005 Afar rift crisis in East Africa), or variations in rock strength along the rift. Our results provide new information on how past dike injection events accommodate long-term plate spreading, as well as providing more details on the Krafla rift crisis. This study also highlights the potential of optical image correlation using inexpensive declassified spy satellite and aerial photos to measure deformation of the Earth's surface going back many decades, thus providing a new tool for measuring Earth surface dynamics, e.g. glaciers, landsliding, coastal erosion, volcano monitoring and earthquake studies, when InSAR and GPS data are not available.

Citation: Hollingsworth, J., S. Leprince, F. Ayoub, and J.-P. Avouac (2012), Deformation during the 1975–1984 Krafla rifting crisis, NE Iceland, measured from historical optical imagery, *J. Geophys. Res.*, *117*, B11407, doi:10.1029/2012JB009140.

1. Introduction

[2] With the obvious technical challenges in studying oceanic rift zones directly, our understanding of the processes that operate within rift zones and that influence their topographic and structural evolution remain relatively poor. The interplay between diking and faulting is a key factor controlling the structural development of spreading centers; differences in the amount of plate spreading accommodated by diking versus faulting ultimately lead to the very different topographic expressions of rift zones from around the world [*De Chabalier and Avouac*, 1994; *Buck et al.*, 2006]. Injection of dikes and slip on faults occur as instantaneous events in the geological record. Therefore, geodetic measurements which span a volcanic or tectonic event provide a method for measuring the displacement field associated with that event. Deformation associated with a single volcanic or seismic cycle can then be scaled up to see how it may produce the geological deformation we see preserved in the landscape. Obviously, this can only be achieved where the co-seismic and geologic ground displacements can be measured from remote sensing or geodesy.

[3] Recent studies from Afar and Tanzania have combined local seismicity and radar data to measure the intrusion of dikes where plate spreading is accommodated on land in the East African rift [*Wright et al.*, 2006; *Baer et al.*, 2008; *Calais et al.*, 2008; *Biggs et al.*, 2009; *Grandin et al.*, 2010b]. Along with dike injection during the 1978 Asal rifting crisis [*Abdallah et al.*, 1979; *Ruegg and Kasser*, 1987; *Cattin et al.*, 2005], these three rare examples show how long-term plate spreading in the East African rift is accommodated by short-term episodic dike injection.

[4] The only other region where plate spreading occurs on land, and may therefore be imaged geodetically, is Iceland. Recent injection of a dike in an off-rift setting in southern Iceland resulted in the Eyjafjallajökull eruption, the ash clouds from which caused major disruption to European air traffic in spring 2010 [*Sigmundsson et al.*, 2010]. Although no inner-rift dike injections have occurred in Iceland in the period of GPS and InSAR observation (1990s and later), a major volcanic episode occurred between 1975–1984, known as the Krafla rifting crisis, or 'Krafla Fires', during which around 20 dikes were injected into the crust within the Northern Volcanic Zone (NVZ) of NE Iceland (Figure 1) [see also *Tryggvason*, 1984; *Björnsson*, 1985; *Sigmundsson*,

[1]Division of GPS, California Institute of Technology, Pasadena, California, USA.

Corresponding author: J. Hollingsworth, Division of GPS, California Institute of Technology, MC 100–23, Pasadena, CA 91125, USA. (james@gps.caltech.edu)

0148-0227/12/2012JB009140

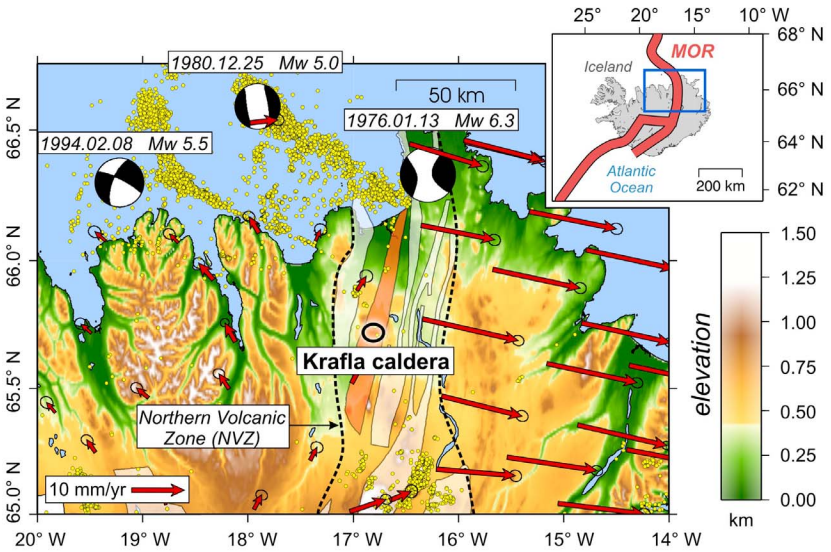

Figure 1. Topographic map of the northern central region of Iceland (inset figure shows the location within the wider mid-Atlantic plate spreading zone). Yellow circles show the location of micro-earthquakes ($M_w \geq 2.8$) between 1990–2010 from the SIL earthquake catalog of the Iceland Meteorological Office (http://hraun.vedur.is/ja/google/index.html). Red arrows show GPS velocities from *Árnadóttir et al.* [2009] relative to stable North America. Black earthquake focal mechanisms are earthquake centroid determinations from the Harvard CMT catalog. Heavy dashed black lines show the boundaries of the Northern Volcanic Zone (NVZ), across which all the plate spreading between Eurasia and North America is accommodated at this latitude. Transparent white areas highlight the various fissure swarms which lie within the NVZ, which accommodate this plate spreading through a combination of fault slip and magmatic injection. The red area highlights the Krafla fissure swarm, which was active through a number of dike injections between 1975–1984, an event known as the Krafla Fires. The heavy black circle shows the location of the Krafla caldera, which was the focus of much of the Krafla Fires activity.

2006; *Buck et al.*, 2006]. Geodetic measurements of surface extension from triangulation and EDM data were very limited in the early stages of the crisis, during which dikes were injected at depth with relatively little material erupted at the surface. Although surveying of the Krafla caldera, which lies at the southern end of the dike-affected region, increased during the latter stages of the crisis, our knowledge of the spatial extent of opening for the whole region, particularly in the north, remains poor.

[5] In this paper, we use sub-pixel correlation of recent SPOT5 satellite data with declassified US spy images from the 1970s and historical aerial photos from the 1950s, 1960s, 1970s, and 1990s to measure the horizontal displacement field produced during the 1975–1984 Krafla rifting crisis. This allows us to significantly revise the location, magnitude, and evolution of opening, as well as investigate the interaction between magmatic (i.e. dike) and tectonic (i.e. fault) deformation in this rifting episode. We first outline the procedure for producing displacement maps from optical images, before discussing the results and the main implications for deformation during the Krafla Fires. We build on these observations in a second paper (J. Hollingsworth et al., Structural constraints for the 1975–1984 Krafla rifting crisis, NE Iceland, from optical imagery and survey data, submitted to *Journal of Geophysical Research*, 2012), which focuses on modeling of the optical displacement data to determine the best-fitting dike injection and surface faulting parameters throughout the various dike injections and surface faults activated.

2. Overview of the 1975–1984 Krafla Rifting Crisis

[6] Deformation during the 1975–1984 Krafla Fires was accommodated by diking at depth, and faulting/fissuring near the surface. Opening was confined to a 2–5 km wide zone characterized by clear NNE-SSW striking normal faults which offset post-glacial lavas throughout the NVZ (Figure 2). Modeling dike propagation in the Krafla region, *Buck et al.* [2006] produced a similar pattern of dike injections away from a magma chamber as those measured during the Krafla Fires [*Einarsson*, 1991]. However, the magnitude and distribution of opening were both significantly smaller and more uniform than was measured during the Krafla Fires. Furthermore, the first, and largest dike injection could not be modeled with the same parameters as the subsequent dikes. This suggests that either the modeling was too simplistic, which the authors acknowledge, or the measurements of total opening were incorrect, or both.

[7] Although geodetic measurements of deformation from triangulation, EDM, tilt and leveling surveys were made throughout the Krafla Fires crisis [e.g., *Wendt et al.*, 1985; *Tryggvason*, 1984, 1994], the spatial coverage of measurements is very sparse, and almost completely confined to the

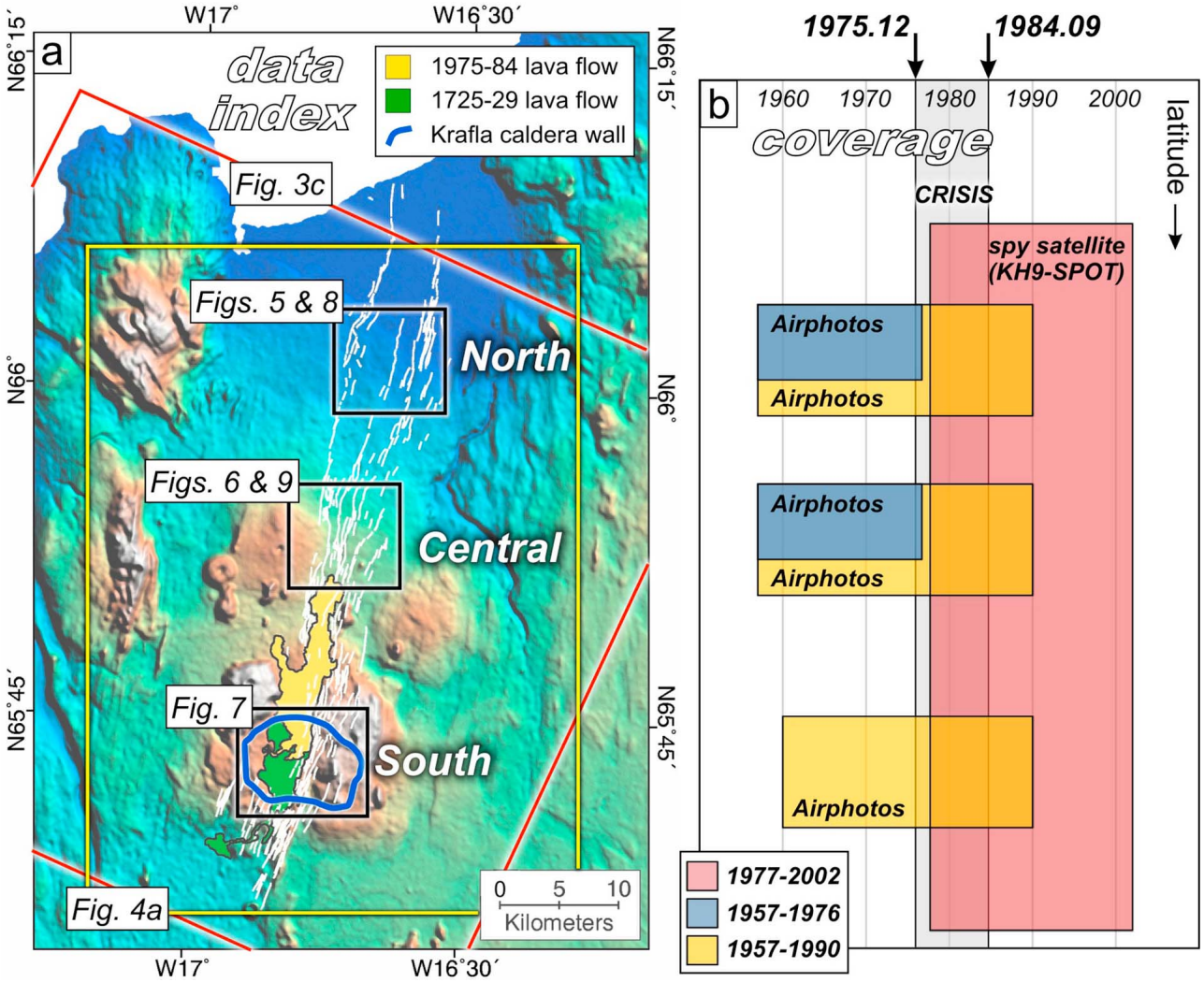

Figure 2. (a) Topographic map of the Krafla region of NE Iceland. White lines show various faults and fissures active throughout the Late Quaternary. Blue circle shows the boundary of the Krafla caldera [from *Björnsson et al.*, 1977], which is thought to have formed during the last interglacial (Eemian) period (114–130 kyr) [*Brandsdotttir et al.*, 1997]. Yellow and green areas show the extent of lava flows during the 1975–1984 and 1725–29 eruptions, respectively [*Björnsson et al.*, 1977]. Large red box shows the footprint of the SPOT5 satellite image correlated with a KH-9 hexagon spy satellite image from 1977 (the footprint of which covers an even larger area than shown in this figure). Black boxes show the location of aerial photo correlations throughout this study. (b) Plot showing the spatial and temporal coverage of the different data sets used to constrain opening during the 1977–1984 Krafla rifting crisis. The gray zone shows the duration of the crisis.

southern region around the caldera itself, thereby preventing a more detailed investigation of how plate spreading is accommodated by dike injection. Measurements from the northern and extreme southern ends of the fissure swarm are generally poorly constrained, although some individual dike injections from these regions have been studied in detail, providing some information on the geometry of diking and faulting [*Rubin*, 1992]. *Buck et al.* [2006] provides a most comprehensive summary of events throughout the crisis; the onset of activity was signaled by intense seismicity in the Krafla region on the 20th December 1975, coupled with significant tilting and eruption of volcanic material within the caldera [*Björnsson et al.*, 1977]. Seismic activity remained high until January-February 1976, with much of the activity confined to the caldera itself. However, the largest earthquake of the entire crisis occurred on the 13th January (M_w 6.3) at the northern end of the rift zone, some 60 km north of the caldera. This earthquake occurred offshore in the Axarfjördur region (Figure 1). The right-lateral focal mechanism suggested slip on a NW-SE transform fault, in response to NW-SE extension in the south resulting from dike injection.

[8] Once the majority of extension had been relieved by dike injections at mid-to-shallow crustal levels, increasing amounts of magma were erupted throughout the crisis, mostly in the vicinity of the caldera. The crisis ended with its most extensive eruption, occurring between 4–18th September 1984, which covered the caldera-region and extended 10 km to the north (Figure 3c).

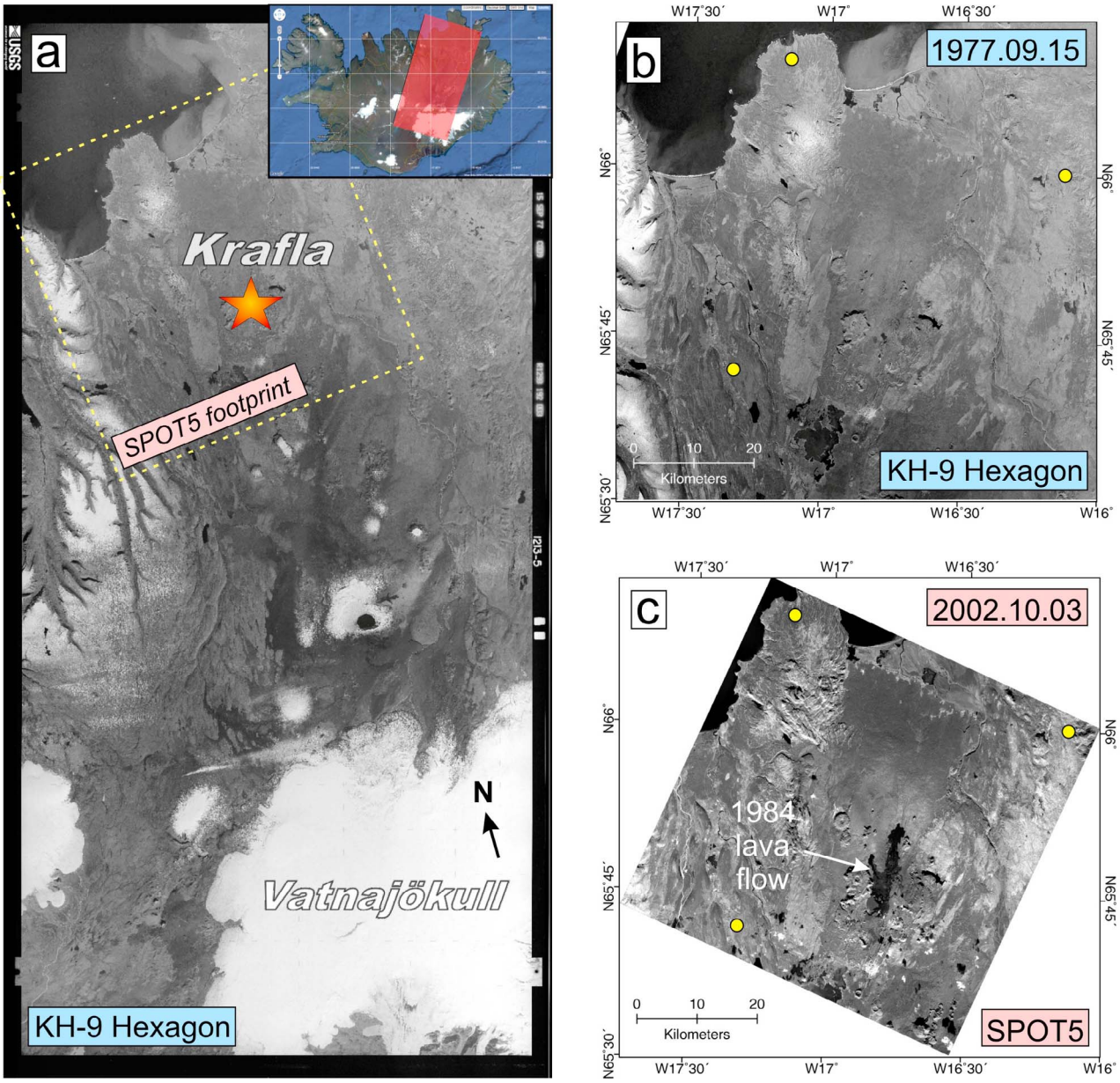

Figure 3. (a) KH-9 Hexagon satellite image of the Krafla region, NE Iceland, acquired on the 15th September 1977. Orange star shows the location of the Krafla caldera. Dashed yellow box shows the 60 × 60 km footprint of the post-crisis SPOT5 image. The white region in the SE of the image is the Vatnajökull ice cap. Inset shows the footprint of the KH-9 image relative to Iceland. (b, c) Overlapping regions of the KH-9 and SPOT5 images are shown in Figures 3b and 3c, respectively. Yellow circles show the location of tie points used to co-register the KH-9 and SPOT5 images. Lavas erupted near the Krafla caldera in 1984 are only visible in the post-crisis SPOT5 image.

[9] Between 1975 and 1984 around 9 separate eruptions occurred and 20 dikes were injected into the crust, which resulted in 9–10 m of surface opening near the caldera [*Wendt et al.*, 1985; *Tryggvason*, 1984; *Árnadóttir et al.*, 1998; *Buck et al.*, 2006]. However, since the region of diking extended more than 50 km north and 10–20 km south of the caldera, our knowledge of the distribution of opening along the whole length of the fissure swarm remains poor. The aim of this paper is to revise current estimates of opening over the entire Krafla rift, using new measurements from correlation of optical satellite and aerial photo data.

3. Methods: Optical Correlation of Spy Satellite and Aerial Photos

[10] Correlation of both satellite and aerial images have been successfully used to identify co-seismic ground ruptures and quantify fault offsets during large earthquakes [*Michel*

and Avouac, 2002, 2006; *Avouac et al.*, 2006; *Copley et al.*, 2011; *Wei et al.*, 2011], and the displacement field produced by injection of magmatic dikes [*Barisin et al.*, 2009; *Grandin et al.*, 2010a]. While previous studies have focused on using modern satellite data such as SPOT and ASTER imagery, we discuss a new procedure for co-registering and correlating older KH-9 spy satellite and aerial photos for the purposes of measuring ground displacements. In the following section we discuss the key aspects of this new procedure which are relevant to the results and discussion sections of this study. However, further details on the methodology may be found in Appendix A.

3.1. Orthorectification and Correlation of KH-9 and SPOT5 Satellite Images

[11] We measure the displacement field associated with the 1975–1984 Krafla rift crisis using the COSI-Corr software package (freely available from www.tectonics.caltech.edu/slip_history/spot_coseis/index.html), which compares two images of the Earth's surface that were acquired at different times, and measures any pixel shifts between them with an accuracy around 1/10 of the input image pixel size. Although this technique was developed primarily for use with modern pushbroom satellite systems, recent development has enabled its use for correlating aerial photos [*Ayoub et al.*, 2009]. *Surazakov and Aizen* [2010] recently showed that declassified KH-9 Hexagon US spy images could be treated as very high altitude aerial photos for the purposes of orthorectifying, which resamples the image to account for any topographic component in oblique view images — for more details on the orthorectifying procedure, see Appendix A1. For these purposes, information about the camera system is required, such as focal length, optical distortions, and film size, and which currently remains classified for all declassified US spy images. After experimenting with different camera parameters, *Surazakov and Aizen* [2010] concluded that KH-9 images were acquired with a similar camera system as the NASA Large Format Camera (LFC) [see *Mollberg and Schardt* 1988]. Therefore, we use the LFC focal length of 30.5 cm, and define the extents of the image using the 1×1 cm grid of reseau points which cover the image. KH-9 images were acquired globally between 1971 and 1980; each image footprint measures 250×125 km, with a resolution of 6–9 m, and may be purchased from the USGS (earthexplorer.usgs.gov) for $30.

[12] Figures 3a and 3b show a KH-9 Hexagon spy satellite image covering the NE Iceland region, acquired on the 15th September 1977. This image was correlated with a SPOT5 pushbroom satellite image of the Krafla region acquired on the 3rd October 2002 (Figure 3c). The SPOT5 image is first orthorectified with COSI-Corr using georeferencing information contained within the accompanying header (or 'dim') file, and a 30 m ASTER Global DEM. The KH-9 Hexagon image is then co-registered to the SPOT5 orthorectified image using 3 tie points collected 20–30 km from the deforming region (Figure 3b). Because we do not have a pre-crisis DEM, the KH-9 image is then orthorectified with the same post-crisis ASTER GDEM. The KH-9 and SPOT5 orthoimages are shown in Figures 3b and 3c. The uniform black area which strikes northward from the caldera in the post-event SPOT5 image corresponds to the 1981 and 1984 lava flows.

[13] Correlation of the KH-9 and SPOT5 orthoimages is performed using COSI-Corr, which outputs E-W and N-S displacement maps showing how the pixels move between the two image acquisitions. A multiscale sliding correlation window of 64 to 32 pixels is used, with a measurement made every 8 pixels (64 m). This method matches groups of pixels based on their frequency content, and is typically more accurate than matching based on gray scale value. Displacements can be resolved down to 1/10 of the input pixel size, i.e. $\sim$1 m for KH-9 images. For further details on the correlation method, see *Leprince et al.* [2007].

3.2. Removal of Non-tectonic Noise From KH-9 and SPOT5 Correlation Map

[14] In contrast with pushbroom satellite images, film-based satellite images are subject to additional sources of error resulting from film-distortions, scanning of the film, and inadequate knowledge of the camera system used to acquire the images. These effects may produce signals which overprint the tectonic signal in displacement maps, albeit at wavelengths usually longer than the short-wavelength deformation produced by localized surface slip, i.e. across fault ruptures.

[15] Topography unaccounted for by the DEM during the orthorectification process may result in an additional source of noise present in the correlation maps. Residual short-wavelength topographic signals may remain in the correlation map, and can significantly overprint the displacement field. This problem occurs if the two images are acquired with an oblique view component, and the DEM's used to correct them are of lower resolution than the input satellite images, e.g. $\sim$8 m KH-9 images orthrectified with a 30 m ASTER GDEM (Version 1). In these cases, there is a stereo effect between the two images, which records the surface topography, and which is not corrected by the coarser DEM — it is this principle which allows DEM's to be extracted from stereo imagery. Because the topographic signal between the two images is greatest in the direction of stereo overlap, known as the epipolar direction or plane of parallax, and negligible in the direction perpendicular to this, we can project our displacement maps into the epipolar-perpendicular direction to retrieve a displacement signal with minimal topographic residuals. For more details on the procedure for removing topographic residuals from displacement maps, see Appendix A2. Topographic residuals may also occur if the topography moves significantly between image acquisitions, and the same DEM is used to orthorectify both images. This effect is particularly strong with large lateral ground displacements in hilly or mountainous terrain [*Ayoub et al.*, 2009; *Oskin et al.*, 2012].

[16] Other factors may also affect the correlation of pre- and post-crisis images, such as quality of the film, changes in vegetation, differences in sun shading, presence of snow, deposition of sediment, erosion, anthropogenic effects, and various other processes which change the Earth's surface. These may combine in ways which act to hinder the correlation (e.g. it may be hard to correlate a snowy image with a non-snowy image), or may produce a directional bias in the correlation, thereby complicating the tectonic signal (e.g. different sun shading may bias the correlator in the direction of the shadows). Such effects vary between different images, and may be difficult to remove from the final displacement map, especially if their effects are very small, and non-

uniform across the image. Nevertheless, even the qualitative recognition of these various factors may help in assessing the quality of a correlation.

3.3. Orthorectification and Correlation of Historical Aerial Photos

[17] Unfortunately, there are no KH-9 satellite images available which pre-date the rift crisis onset in 1975. To assess opening across the rift zone over the entire crisis (1975–1984), we correlate aerial photos acquired in 1957 and 1960, with photos from 1990, acquired after the crisis ended. Aerial photos were purchased from the National Land Survey of Iceland (www.lmi.is). Because the ground footprint of these photos are relatively small (8 km), we cannot recover the long-wavelength deformation because the images do not extend into the non-deforming regions. Nevertheless, correlation of aerial photos can still provide accurate measurements of the short-wavelength displacement produced by faults [*Ayoub et al.*, 2009]. Furthermore, very precise measurements of the displacement field can be obtained with aerial photos due to their relatively high resolution compared with satellite imagery; *Ayoub et al.* [2009] are able to resolve fault displacements of only 20 cm for aerial photos correlations covering the 1992 Landers earthquake. Therefore, by correlating pre- and post-crisis aerial photos we are able to resolve the total surface opening produced during the crisis, where it is localized onto major faults and fissures (Section 4). We also correlate pre- and inter-crisis aerial photos to examine the displacement field resulting from the early stages of the crisis, which is less well understood.

[18] The method for co-registering and correlating aerial photos is similar to KH-9 Hexagon spy images; both data sets must be orthorectified using the 'Aerial Imagery' module within COSI-Corr, see Appendix A3 for more details. However, because aerial photos are often high resolution, typically $\leq$1 m, topographic residuals are correspondingly very large in the absence of a high-resolution DEM to orthorectify the photos. Therefore, we project all aerial photo correlations into the epipolar-perpendicular direction to minimize topographic residuals.

[19] Furthermore, because a typical aerial photo is acquired at elevations of $\sim$5 km, the resulting image footprint covers an area of $\sim$10 $\times$ 10 km. Because the width of the Krafla rift zone is around 5 km wide, the camera incidence angle varies significantly over the deforming region — although KH-9 images are subject to similar variations in incidence angle, they are acquired at much higher altitudes of $\sim$166 km, resulting in much larger footprints of 250 $\times$ 125 km; therefore the incidence angle varies only a small amount over the 5 km wide Krafla rift. As the incidence angle increases away from the center of an aerial photo, it gains a significant oblique component around the edges of the photo. Therefore, in the absence of a high resolution pre- and post-crisis DEM for orthorectification, some care is needed when interpreting an aerial photo correlation map, because vertical deformation around the edges of the image may produce an apparent horizontal displacement signal — this problem is discussed further in Appendix A4. In the case of the Krafla rift, vertical displacement on the rift-bounding normal faults may slightly enhance, rather than cancel out, the values of horizontal extension at the margins of the correlations, which is where the incidence angles are greatest (i.e. the displacement will include both horizontal and vertical components). This is because the photos were acquired from a flight line which lies in the middle of the rift, and so the camera looks westward at the western rift boundary and eastward at the eastern boundary. Therefore, the fault displacements we measure from correlation of aerial photos are likely to be maximum values.

4. Measuring Krafla Surface Extension

[20] The results of our optical image correlation analysis is presented in the following section. Figure 2 outlines the spatial and temporal coverage of data used in the analysis, and provides an index for the various figures in this section.

4.1. Estimates of Mid-late Crisis Rift Extension: 1977–2002

[21] Figure 4 shows the surface extension across the Krafla fissure swarm between 1977 and 2002. Due to the proximity of the tie points to the rift zone (Figure 3), particularly east of the rift, artifacts related to scanning, and the lower image quality of the KH-9 compared to the SPOT5 image, the long wavelength decay of the horizontal displacement signal and the quality of the co-registration may be slightly biased. Nevertheless, the relative displacements across discontinuities are well resolved [see also *Ayoub et al.*, 2009].

[22] The majority of extension is accommodated on rift bounding faults and fissures. The width of the rift increases from $\sim$1 km in the south, to $\sim$5 km in the north. Although the spatial and displacement resolution of the KH-9-SPOT correlation is too low to resolve details of inner rift extension, the relatively smooth displacement profile across the inner rift for the northern section of the swarm suggests little or no extension is accommodated by localized faulting or fissuring between the rift bounding faults. Virtually all of the extension is accommodated on the rift-bounding faults shown as black lines in Figure 4a. Surface extension across the rift varies between 4–5 m, and is relatively uniform along the rift zone, with slightly elevated opening in the central section. The presence of the river delta at the northern end of the rift results in poor coherence, thus preventing the measurement of extension near the coastline. A kink in the strike of surface opening occurs in the middle of the rift (Figure 4a), and corresponds to a similar kink in the migration of seismicity during the July 1978 earthquake swarm [*Einarsson and Brandsdottir*, 1980].

4.2. Estimates of Total Rift Extension: 1957–1990

4.2.1. Northern Rift-Segment

[23] Correlation of aerial photos from 1957 and 1990 for the northern section of the Krafla fissure swarm, near the Axarfjördur coastline, are shown in Figure 5. Both image correlations are produced from overlapping 1957 and 1990 aerial photos taken along N-S flight lines. In each case, pre- and post-crisis images were co-registered using tie points collected from the eastern rift flank, which is assumed to be stable. Displacement values are given in the epipolar perpendicular directions, shown by the black arrows, which are

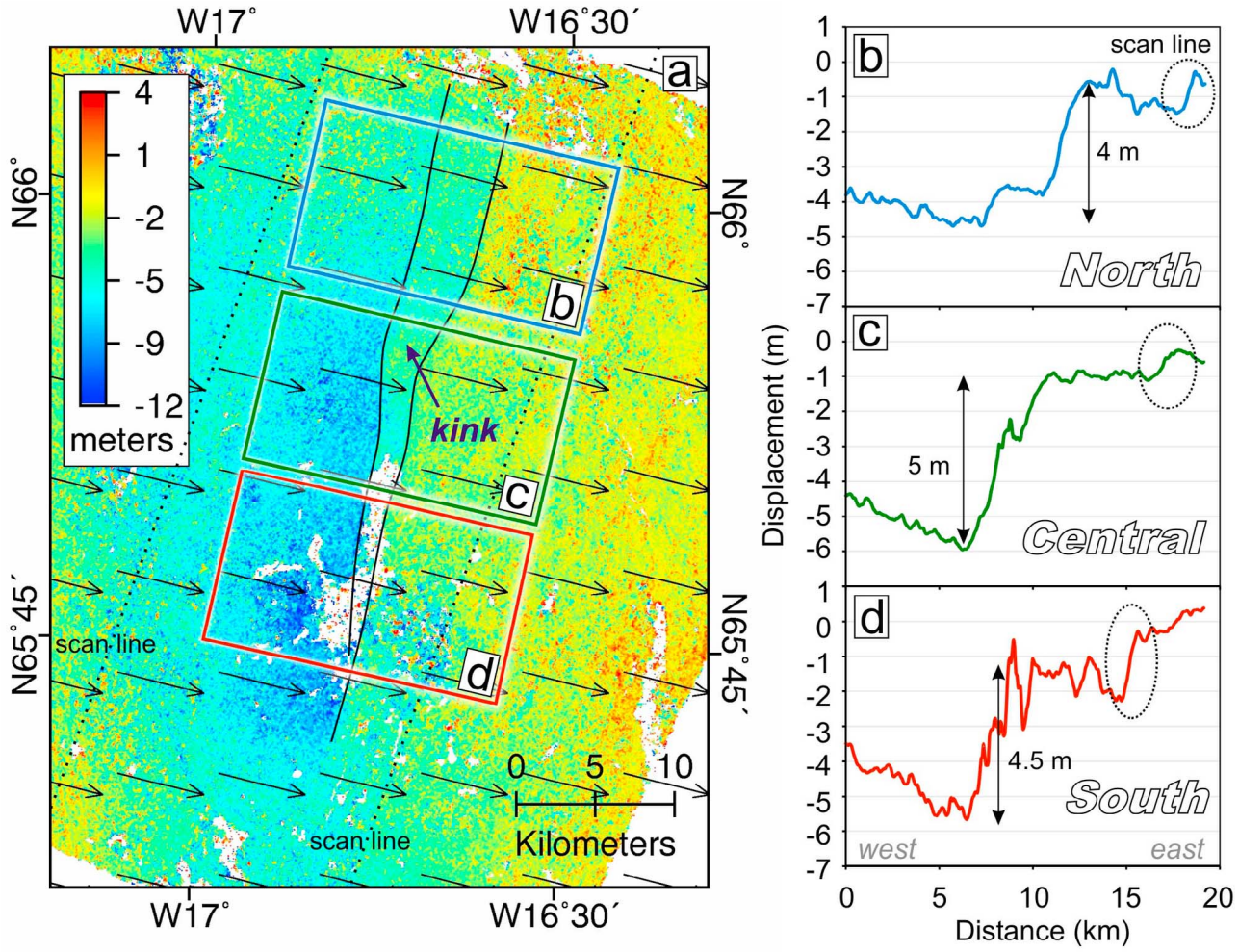

Figure 4. (a) Reprojection of the epipolar perpendicular displacement field into the 104° direction (i.e. perpendicular to the strike of the rift zone) — see Figure 2 for location. Black lines show the simplified location of rift bounding faults which were activated between 1977–2002. Blue arrow shows a kink in the strike of the rift bounding faults. Dotted black lines show steps in the displacement field which result from film scanning artifacts. Stacked displacement profiles are shown across the (b) north, (c) central, and (d) southern parts of the rift zone. Displacement values are relative to the tie point locations (Figures 3b and 3c); because the tie points do not extend far enough from the rift zone, the values are not absolute, but relative. Dotted black circles show steps in the displacement field produced by scanning artifacts.

free from topographic residuals and approximately perpendicular to the faults/fissures within the fissure swarm. It is necessary to look at displacement in the epipolar perpendicular direction because the aerial photos (0.5 m resolution) are orthorectified with the much coarser ASTER GDEM, and so the raw E-W and N-S displacement fields output by COSI-Corr are obscured by topographic residuals.

[24] Figures 5b and 5d show swath profiles of displacement across the rift zone, taken approximately perpendicular to the fissure swarm and sub-parallel to the epipolar perpendicular direction. The positive signal within the middle of the rift zone is likely an artifact produced by subsidence in the left side of the image, which is viewed obliquely by the camera, and then orthorectified using the post-crisis DEM (see Appendix A4 for more details). The eastern rift flank is fixed between both images, yielding approximately zero horizontal displacement. Discontinuities in the displacement field indicate extension accommodated on faults/fissures. The northern-most correlation (Figure 5a) only just spans the entire rift, which is widest (~5 km) at this latitude. Approximately 2.0–2.5 m extension is accommodated across a 1.5 km-wide distributed zone of faults/fissures forming the eastern margin of the rift zone, while 1.0–1.5 m extension is accommodated on a fault/fissure forming the western margin of the rift. Decorrelated areas occur due to rapid temporal changes in the river delta. Vertical displacements do not contribute significantly to the horizontal displacement values from the center of the correlation, because the incidence angles from the pre- and post- images are close to nadir (see Appendix A4). The incidence angle at the western edge of the image is 25–30°, and so a vertical displacement of 2.2–3.3 m could produce an apparent westward displacement of 1.0–

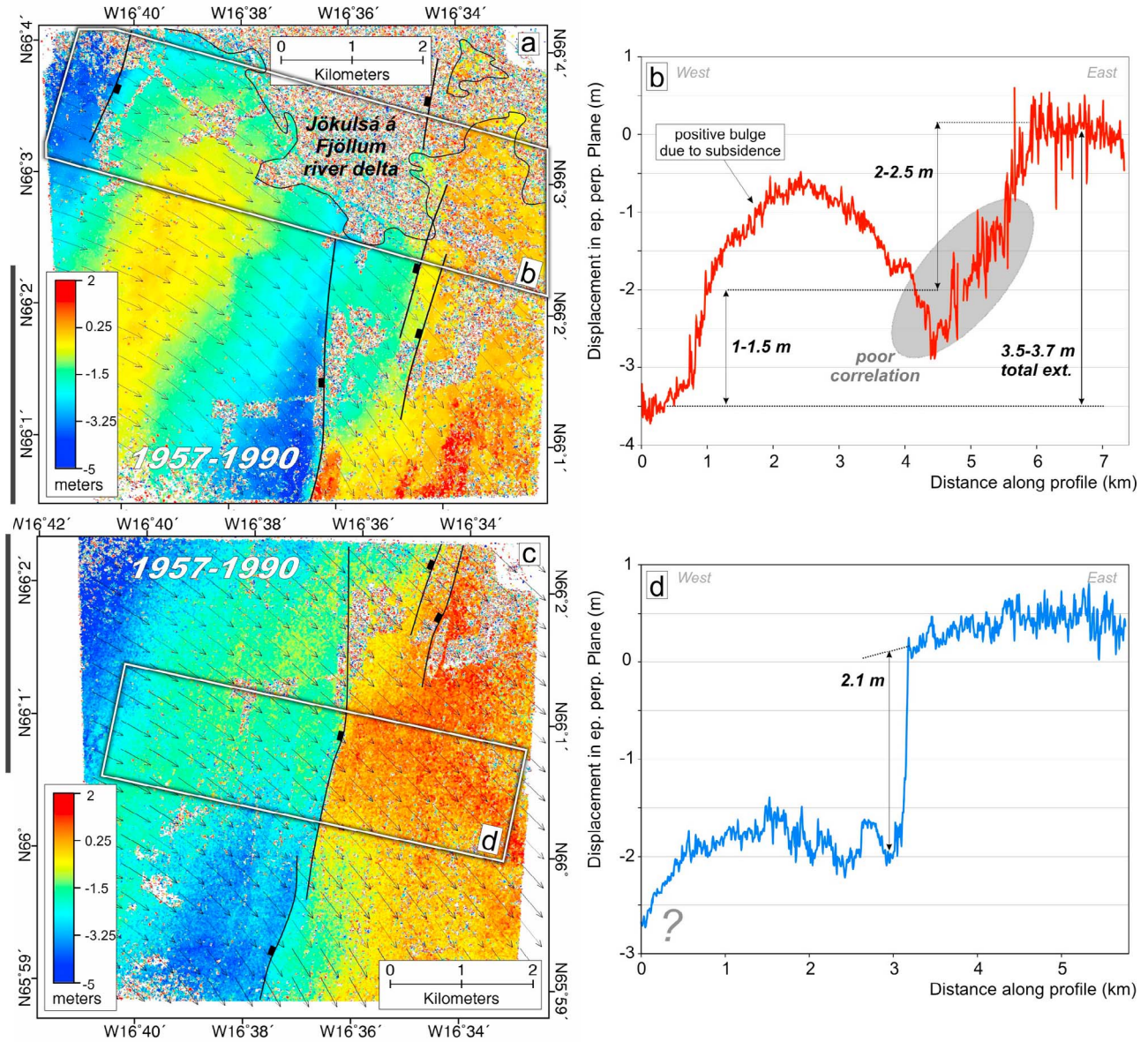

Figure 5. (a) Epipolar perpendicular displacement field for the northern end of the Krafla fissure swarm (see Figure 2 for location) from 1957 and 1990 aerial photos. Decorrelated areas in the north of the image coincide with the Jökulsá á Fjöllum river delta. Black lines show normal faults which moved during the crisis. Tie points were collected from the eastern rift flank. (b) Swath profile of the deformation across the rift zone (shown by the white box in Figure 5a). Although the swath crosses the river delta, it is the only profile to span the entire northern section of the rift. The relative displacements across faults are robust, while distributed deformation is hard to distinguish from displacement ramps introduced by misregistration of the pre- and post-crisis images (see Appendix A4). Gray area is poorly constrained due to low coherence. (c) Epipolar displacement map. (d) Displacement profile for the region immediately south of Figure 5a. The displacement maps in Figures 5a and 5c overlap in the areas shown by the black bars on the left side of the image.

2.5 m. Alternatively, the same signal could be produced by pure horizontal displacement, or some combination of horizontal or vertical motion; equal values of 0.8 m vertical and horizontal slip could constructively produce 1.2 m westward motion. Therefore, a horizontal displacement of 1.5 m is likely to represent a maximum value. The 4–5 km width of the rift is the same as seen on the KH-9-SPOT5 correlation in Figure 4. The total extension accommodated at the surface is 3.5–3.7 m; less than the 5.5–7 m estimated by *Tryggvason* [1984]. However, it should be noted that due to the small 6 km swath size of the aerial photos, we are less sensitive to long-wavelength distributed deformation, which could account for some of this difference.

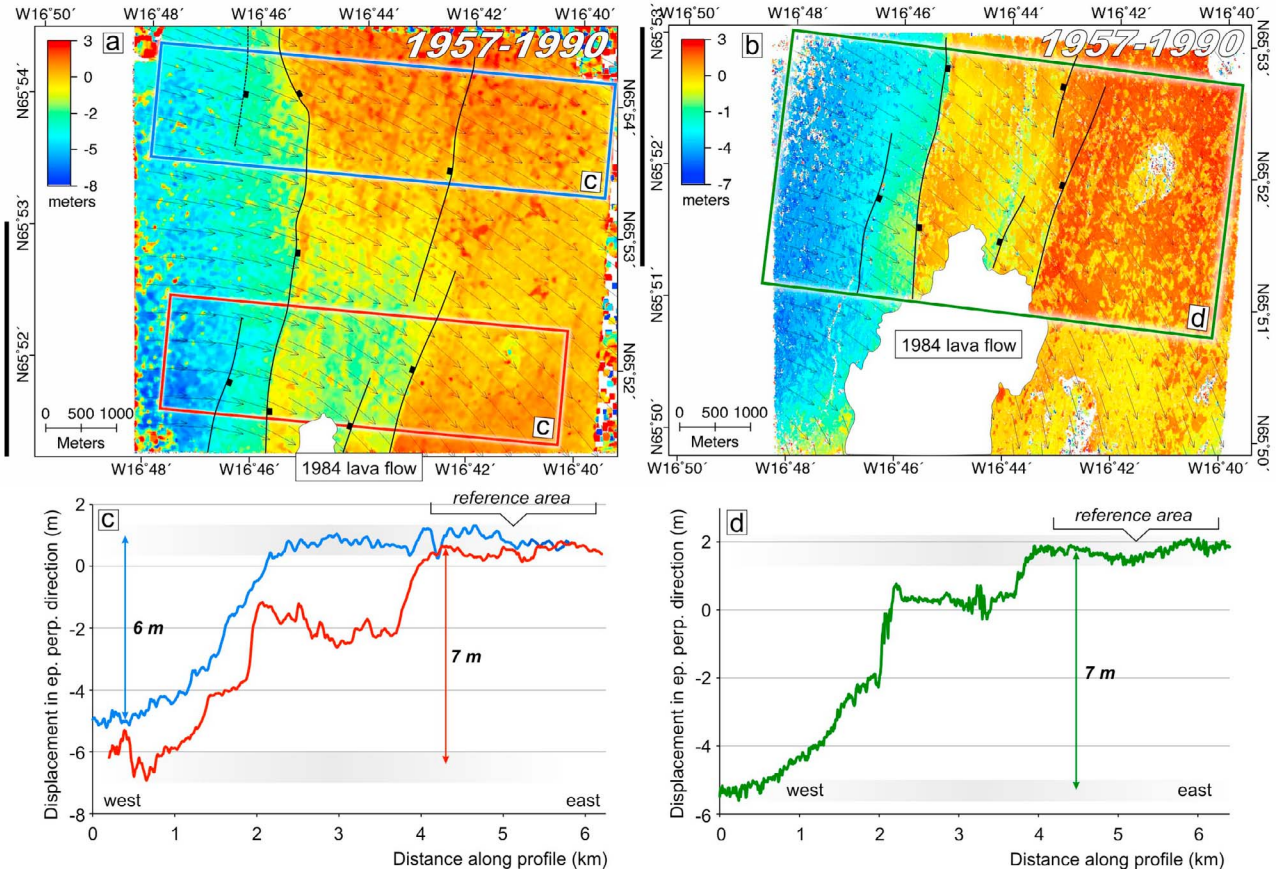

Figure 6. (a and b) Epipolar perpendicular displacement fields for the central section of the Krafla fissure swarm (see Figure 2 for location) from correlation of 1957 and 1990 aerial photos. Decorrelated areas in the south of the images are due to lavas erupted in 1984. Black lines show normal faults which moved during the crisis. Displacement values of ~2 m for the reference region in Figure 6b result from problems co-registering the two images, due to fattening effects (see text for details). The two displacement maps overlap in the areas shown by the black side bar. (c and d) Swath profiles of the rift-perpendicular deformation, shown by the blue and red boxes in Figure 6a, and the green box in Figure 6b.

[25] Figure 5c shows a correlation immediately south of Figure 5a. Only the central and eastern parts of the rift zone are covered by the correlation, and so the total extension cannot be resolved here. Nevertheless, extension on the eastern rift margin is well resolved at 2.1 m, consistent with the 2.0–2.5 m estimate from Figure 5b. Deformation becomes more localized to the south. Because the epipolar perpendicular direction in Figures 5a and 5c contains a large N-S component, slip on normal faults will produce subsidence and thus a northward signal in the rift zone for the southern part of the correlation (negative/blue epipolar perpendicular displacement), and a southward signal for the northern part of the correlation (positive/red displacement). See Appendix A4 for more details. For the west and east parts of the correlation, subsidence will produce eastward (positive) and westward (negative) motion respectively. This effect is the likely cause of the positive bulge in the middle of the rift zone in the Figures 5b and 5d profiles. Nevertheless, the displacement values for the western rift flank in Figure 5b begin to flatten out, suggesting no more localized deformation is occurring outside the rift zone, consistent with the KH-9-SPOT5 correlations. If we assume the relative elevations of the east and west rift flanks have not changed significantly throughout the crisis, i.e. minimal relative subsidence/uplift between the rift flanks, which is also consistent with the long term geomorphology, then 3.5–3.7 m difference between the east and west flanks reflects the maximum total horizontal extension.

4.2.2. Central Rift-Segment

[26] Figures 6a and 6b shows aerial photo correlations for the central section of the Krafla fissure swarm, immediately north of the lava flow which erupted at the end of the crisis in 1984. The eastern rift flank is fixed using tie points. Elevated values in the reference area of Figure 6b are likely a result of fattening effects during the correlation; a defect by which the center of the pixel correlation window inherits the displacement of the more contrasted pixels within the window. However, the relative displacement between the east and west rift flanks is ~6 m at the north of Figure 6a, and ~7 m in the south of Figure 6a and north of Figure 6b, which cover the same area (Figures 6c and 6d). The correlations for this section of the rift zone are relatively noisy, which may

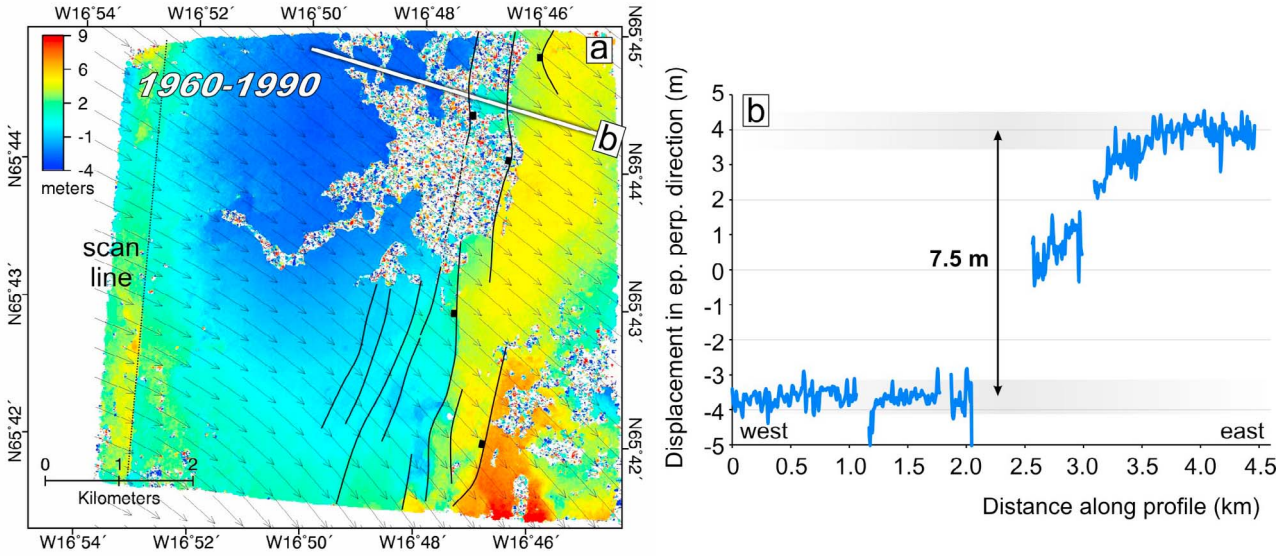

Figure 7. (a) Epipolar perpendicular displacement field for the southern section of the Krafla fissure swarm (see Figure 2 for location) from correlation 1960 and 1990 aerial photos. Decorrelated areas in the north of the image corresponds with the southern limit of the 1984 erupted lavas. Black lines show normal faults which moved during the crisis. (b) Profile of the rift-perpendicular deformation (shown by the white line in Figure 7a).

partly be due to the presence of snow drifts west of the rift zone, which reduce the coherence between the pre- and post-crisis images.

4.2.3. Southern Rift-Segment

[27] Figure 7a shows an aerial photo correlation (1960–1990) for the southern section of the Krafla rift zone, near the southern extent of the 1984 lava flow. The 1960 photo was correlated with the 1990 aerial photo using tie points collected either side of the rift zone; *Ayoub et al.* [2009] showed this approach allows displacements across faults and fissures to be well resolved, although may bias how the deformation signal decays at longer wavelengths. The obvious N-S discontinuity at the western edge of the image is a scanning artifact from the 1960 aerial photo. The rest of the correlation is relatively clean, with a typical noise level of 0.2–0.5 m. A complicated deformation pattern in the south-east corner of the correlation may result from vertical motion on normal faults. Figure 7b shows a displacement profile across the north of the correlation, where patches of high ground remain clear of lava, thereby yielding displacement measurements across the rift. A total of 7.5–8.0 m extension is accommodated across a 1 km wide zone, which represents the peak extension value measured across the whole rift zone. These values decrease to 6–7 m in the south of this figure.

4.3. Estimates of Early Crisis Rift Extension: 1957–1976

4.3.1. Northern Rift-Segment

[28] Figure 8 shows the displacement field for the northern end of the fissure swarm for the early period of rifting, spanning 1957–1976 (same region as Figure 5). Localized extension is clearly resolved at the northern edge of the correlation, close to where the Jökulsá á Fjöllum river delta cuts across the rocky lava flows which characterize the Krafla region; the river deposits do not correlate due to their rapid temporal evolution. Up to 2 m of opening is accommodated on faults/fissures within the delta, consistent with field reports from *Tryggvason* [1976]. However, no obvious opening is present in the correlation maps to the south (Figures 8a and 8c), implying there was no extension on faults/fissures in this region. This pattern is confirmed by swath profiles across the northern (Figure 8b) and southern (Figure 8d) parts of these correlations. Around 0.6–1.1 m opening is accommodated across faults within the northern profile, although this value increases to >2 m further north within the river delta. Fault slip is less clearly resolved on the western rift boundary; the broad increase in westward motion of this rift flank may result from uplift associated with dike injection at depth but with no surface faulting. See Appendix A4 for more details. Little or no localized extension is accommodated on the southern profile. Although image correlation is less sensitive to long-wavelength deformation, any distributed opening across the inner rift would still produce a short-wavelength ramp in the displacement profile, assuming it is accommodated over a few kilometers.

4.3.2. Central Rift-Segment

[29] Figure 9a shows the 1957–1976 displacement field for the central section of the Krafla fissure swarm (same region as shown in Figure 6), 10–15 km north of the caldera. A strong parallax effect between the two aerial photos, as well as snow drifts and low sun illumination in the 1957 photo result in a relatively noisy correlation, especially where a hill occurs in the center-right of the correlation. They may also account for the unexplained long-wavelength signals present across the rift zone, particularly around the edges of the correlation. Nevertheless, the amount of opening across the northern edge of the correlation is small — definitely less than 2 m, as seen at the northern end of the rift — with no obvious sign of localized opening. A possible opening of 1 m

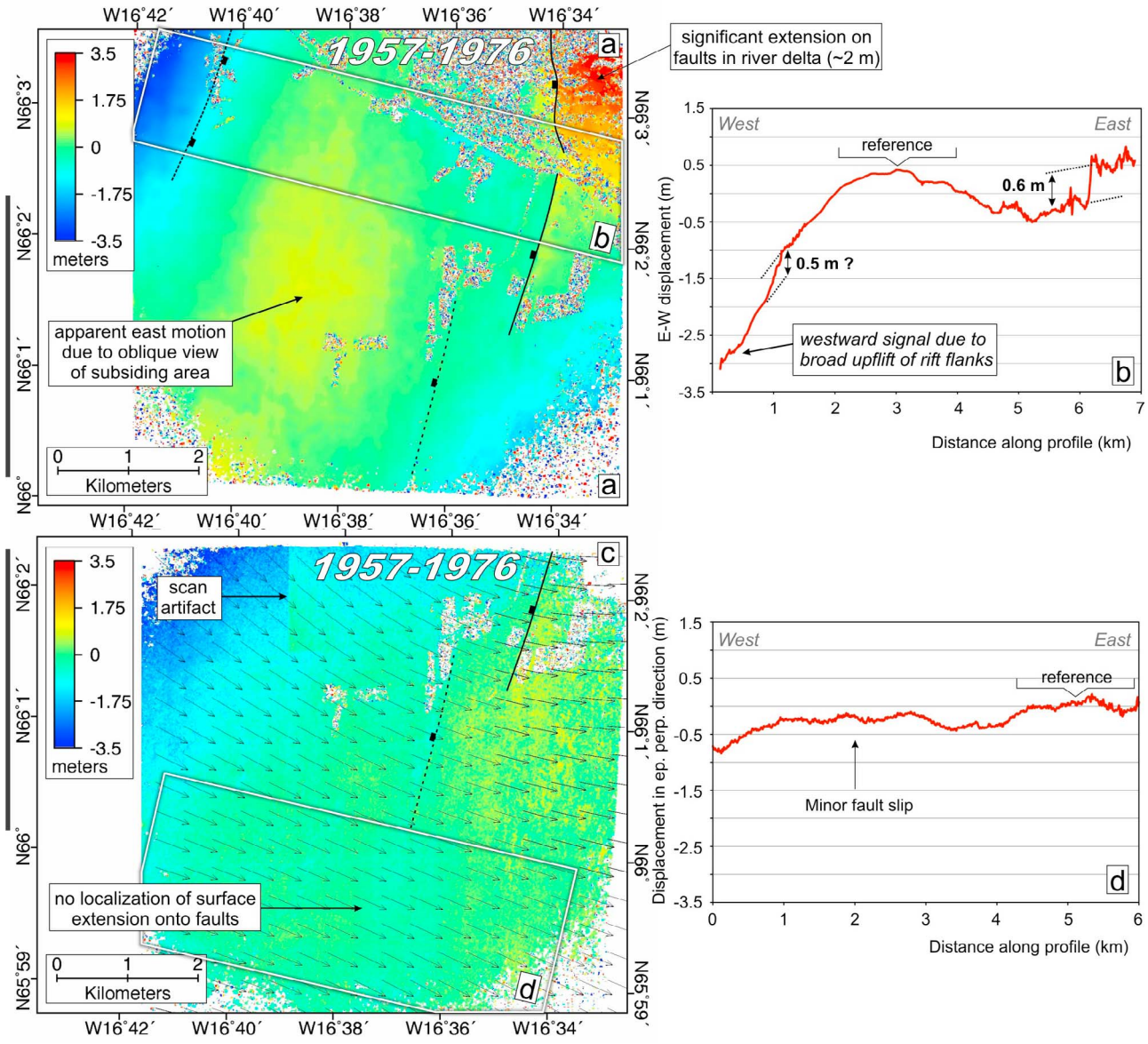

Figure 8. (a) East-west displacement field for the northern end of the Krafla fissure swarm (see Figure 2 for location) from correlation of 1957 and 1976 aerial photos. Because the camera was in the same location for each photo acquisition, there is no parallax difference between the two images and both the E-W and N-S displacement fields are free from topographic residuals. Black lines show normal faults which moved during the early stages of the crisis. The 1976 photo was registered to the 1957 aerial photo using tie points from the middle of the image. (b) A swath profile of the deformation across the rift zone (shown by the white box in Figure 8a). (c) Displacement map, and (d) displacement profile for the region immediately south of Figure 8a. Black side bars show the region of overlap between Figures 8a and 8c. Although the region shown in Figure 8c does not span the entire rift zone, no obvious opening is observed across the eastern rift-bounding fault.

may occur at the southern edge of the correlation, along the western rift boundary, which may relate to dike injection beneath the caldera to the south. However, this opening signal also lies at the edge of the photo, where optical and film distortions are greatest, and coincides with the location of the greatest snow drift. Furthermore, long wavelength uplift of the rift flanks associated with dike injection at depth, but without fault slip at the surface, could result in a smooth westward displacement if the post-crisis DEM was used to orthorectifying both pre- and post-crisis aerial photos (see Appendix A4).

[30] Figure 9c shows a correlation map for the central fissure swarm, but for the 1976–1990 period. The correlation is very clean, and the epipolar perpendicular direction is normal to the faults/fissures bounding the rift zone. A profile of displacement across the rift zone indicates 7 m of opening, with roughly equal opening accommodated on each rift boundary. Because this opening value is the same as that

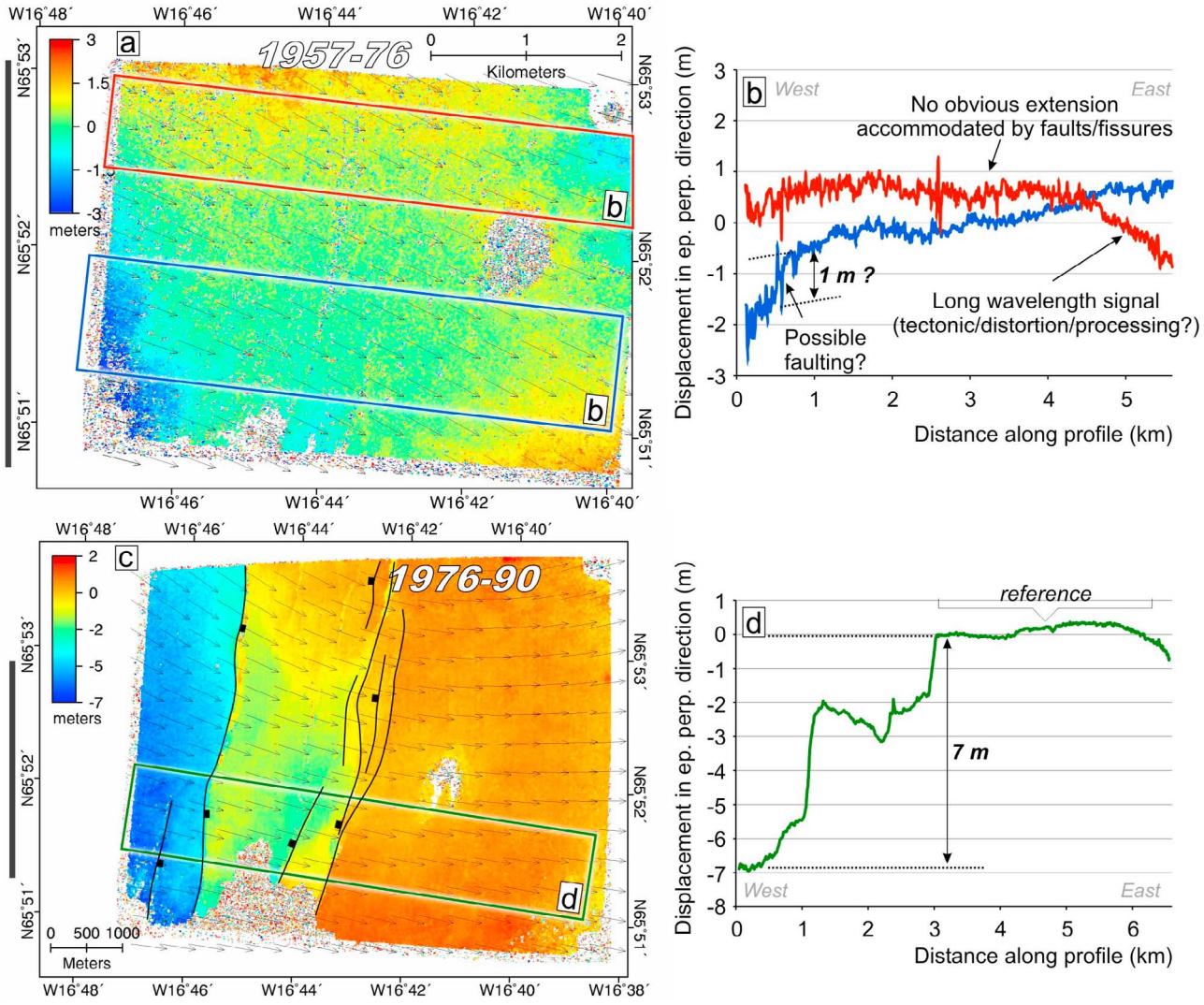

Figure 9. (a) Epipolar perpendicular displacement field for the central section of the Krafla fissure swarm (see Figure 2 for location) from correlation of 1957 and 1976 aerial photos. The 1976 photo was registered to the 1957 aerial photo using tie points collected from the middle of the image, due to a lack of coverage of the rift flanks. (b) Swath profiles across the north and southern regions of the deformation map (shown by the white box in Figure 9a). (c) Epipolar perpendicular displacement field for the period 1976–1990 and (d) displacement profile for the central section of the Krafla fissure swarm, which encompasses the area shown in Figure 8a. The displacement maps in Figures 9a and 9c overlap in the areas shown by the black bars at the side of the image.

measured using aerial photos from 1957–1990 (Figure 6a), it confirms that little or no localized surface opening occurred in the central section of the fissure swarm over a distance of ~20 km between 1957 and 1976.

5. Discussion

5.1. Summary of Opening During the Krafla Rifting Crisis (1975–1984)

[31] A summary of the results presented in Section 4 are shown in Figure 10. The cumulative opening at various stages of the crisis is shown in Figure 11. Our new displacement measurements from optical image correlation indicate a total of ~8 m opening across the Krafla caldera, which is consistent with previous estimates of 9 m for this area [*Tryggvason*, 1984; *Buck et al.*, 2006]. However, our measurements fall short of previous estimates, by 1.5–2.5 m, for the northern part of the rift zone, where total localized extension was at most 3.7 m, based on our image correlation results.

[32] During the period 1975–1984, E-W crustal extension was accommodated by dike injection and fault slip over a distance of ~80 km. Surface extension is accommodated primarily on the rift-bounding normal faults above the dike, rather than by opening of fissures within the rift zone. Average surface opening along the entire 80 km zone of deformation was ~2.5 m for the period 1977–1984, assuming extension decays linearly to zero at the northern limit of the rift zone, near the 1976 earthquake epicenter (Figure 10b). The average surface opening spanning the

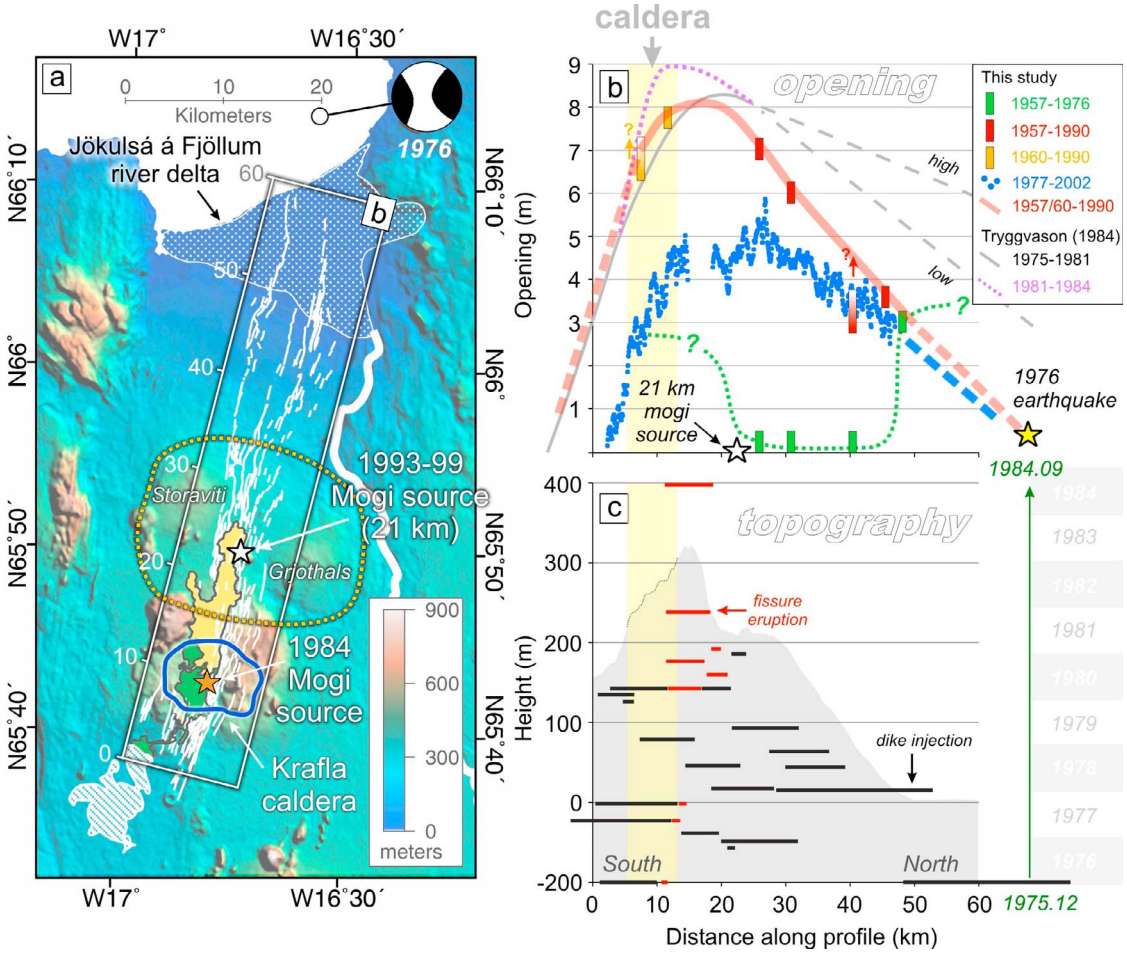

Figure 10. (a) Topographic map of the Krafla region. White lines show faults which have been active in the Quaternary (mapped from aerial photos). Heavy white line and stippled white region show the Jökulsá á Fjöllum river and delta. White dashed region is Myvatn lake. Blue circle shows the Krafla caldera. Orange star is the location of the magma chamber beneath the Krafla caldera from *Árnadóttir et al.* [1998]. White star shows a deeper magma source at 21 km [*de Zeeuw-van Dalfsen et al.*, 2004]. Yellow dotted lines shows a broad zone of uplift comprising the Storaviti and Grjothals topographic highs. The Global CMT solution is shown for the 13th January 1976 earthquake. (b) Profiles of opening (y-axis) along the fissure swarm (x-axis) for the different time periods investigated in this study (see key for details). Grey and purple lines shows the previous best estimate of opening between 1975–1981 and 1981–1984 [*Tryggvason*, 1984; *Árnadóttir et al.*, 1998]. The location along the rift of the 1976 earthquake (yellow star) and 21 km deep mogi source (white star) are shown. (c) Summary of timing and distribution of dike injections and fissure eruptions during the Krafla crisis (adapted from *Buck et al.* [2006]). Grey region shows a swath topographic profile (left y-axis) along the length (x-axis) of the Krafla fissure swarm (swath corresponds to white box in a). Horizontal black and red lines show the location of injected dikes and fissure eruptions (x-axis) and their timing throughout the crisis (right y-axis, time increases vertically from 1975 to 1984 along green arrow). Location of the Krafla caldera is shown by the vertical yellow line in Figures 10b and 10c.

entire rift crisis between 1975–1984 is ~4.3 m along the 80 km length of the rift zone. Therefore, 40% of the total surface opening occurred during the first 20% of the crisis. This is similar to observations from the Afar region of East Africa, where a significant amount of the total opening, >75% at depths of 2–10 km, occurred during the first dike injection [*Grandin et al.*, 2010b]. Opening was not uniform along the Krafla rift zone, with maximum values of ~8 m occurring at the southern end, near the caldera, and ~4 m at the northern end, near the Axarfjördur coastline. This pattern is also similar to Afar, where ~15 m opening occurred in the central section of the rift, and ~5 m occurred at either end of the rift [at depths of 2–10 km, over a distance of 50–60 km [*Grandin et al.*, 2010b]. The distribution of opening along both the Krafla and Afar rift zones correlate with the regional topography, implying a first order link between topography and tectonics, as expected from mechanical analysis of diking (Figures 10b and 10c) [e.g., *Behn et al.*, 2006]. A more complete analysis of the deformation field, which uses elastic dislocation modeling to better constrain

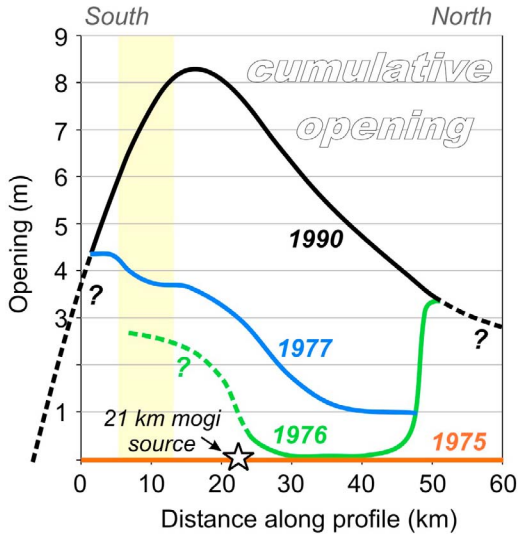

Figure 11. Cumulative opening along the length of the crisis (axes are the same as for Figures 10b and 10c).

the geometry of surface faults and dikes injected throughout the Krafla rifting crisis, is given in Hollingsworth et al. (submitted manuscript, 2012).

[33] In the Axarfjördur coastal region, almost the entire opening during the 9 year crisis was accommodated in the first few months (between Dec 1975 and Sept 1976). Surprisingly, over the same time period, no localized opening is observed along a 20 km section of the fissure swarm between the Krafla caldera and the northern coast (Figures 8 and 9). Although we do not present opening measurements for the southern caldera region during the early stages of the crisis (due to lack of data), significant seismic activity and localized volcanism in this area, coupled with field observations of fault movements within the caldera [*Björnsson et al.*, 1977] suggest localized surface opening occurred at the southern end of the rift zone. Therefore, a bi-modal pattern of opening must have occurred along the fissure swarm during the early stages of the crisis, whereby surface extension was accommodated at the southern and northern ends of the rift, but not in the middle (Figure 10c).

5.2. Implications for the Kinematics of Krafla Dike Injections

[34] If opening at the surface by faulting occurs in response to dike injection at depth, and over similar timescales to dike propagation [e.g., *Hauksson*, 1983; *Rubin and Pollard*, 1988; *Rubin*, 1992], we need to reconcile a bi-modal pattern of surface opening with a magma source which lies at the southern end of the rift zone, where modeling of regional tilt data indicates a magma chamber at 3 km depth beneath the Krafla caldera [*Ewart et al.*, 1991; *Árnadóttir et al.*, 1998] (see also Figure 10a). *Buck et al.* [2006] suggests this pattern could be produced by an increase in tensile stresses away from the magma chamber: a dike would first open near the magma source and propagate laterally, while the driving pressure equals the breakout pressure, but then close up again as it propagated into more tensile regions away from the magma chamber.

[35] One implication of this model is that for a dike to propagate along a crack, and then close up again as it moves along, it must not freeze. However, a dike may have to propagate at depths of >10 km to avoid freezing during propagation; at these depths the host rock temperature is greater than 600°C [*Fialko and Rubin*, 1998]. Because the geothermal gradient likely decreases away from the caldera, the depth at which a dike must propagate to avoid freezing will correspondingly increase. This implies a significant increase in the depth of diking as it propagates away from the 3 km deep magma source near the Krafla caldera. Nevertheless, it should be noted if basaltic dikes inject a rhyolitic crust (rhyolitic volcanism is known from Krafla) [*Jónasson*, 1994], then the dikes could cause melt-back of the host rock, thereby allowing injection at shallower depths. Also, even a partially frozen dike may continue to flow, so long as the constituent crystals do not adhere to the dike walls.

[36] If surface crustal extension is accommodated by normal faults which localize above the shallowest reaches of the dike, where there is a concentration of tensile stresses [*Agnon and Lyakhovsky*, 1995; *Pinzuti et al.*, 2010], the width of the fault-bounded rift zone will reflect the depth to the top of the dike; a wide rift zone results from deep diking, while a narrow rift zone results from shallow diking (assuming a relatively constant fault dip). The Krafla rift zone increases from ~1 km width near the caldera to ~5 km near the coastline, and is consistent with an increase in dike depth as it propagates northward (Figures 4 and 10). However, this observation does not explain the lack of surface faulting along the central section of the rift. First, as the depth to the top of the dike increases northward, the amount of strain at the surface decreases, thereby inhibiting surface slip localization. Secondly, if a dike passes through the central section of the rift without freezing, and yet is wide enough to activate surface faulting north of this section, why does it not activate surface faulting across the central section? Although *Buck et al.* [2006] provide an explanation for dikes closing up at depth, based on a decrease in driving pressure, an additional model is required to explain how surface faults activated by a dike can slip back to their original positions.

[37] An alternative explanation for the bi-modal distribution of surface opening during the early stages of the crisis may be that the strength of the host rock varies along the rift zone. As the driving pressure decreases northward, and the depth to the dike top increases, the deformation is large enough to activate surface faults in the south, but not along the central section of the rift [*Buck et al.*, 2006; *Grandin et al.*, 2012]. However, as the dike injects away from the magma chamber, the pressure in the dike tip cavity is initially maintained by magmatic volatiles. This produces a pore pressure boundary layer in the dike tip, thus preserving low pressure in the host rock and increasing its strength [*Ziv et al.*, 2000]. The southern and central rift segments therefore remain elastic, and the change from surface faulting near the caldera to no surface faulting in the central section is a result of the decreasing driving pressure and increasing depth to the dike top. However, once the dike extends far enough from the magma chamber, the volatiles become fully exsolved from the magma, and the pressure in the dike tip cavity is then maintained by the ambient pore fluid pressure, with influx of fluids from the host rock into the dike tip. This results in a lower frictional resistance at the tip of the dike, causing weakening of the host rock [*Ziv et al.*, 2000].

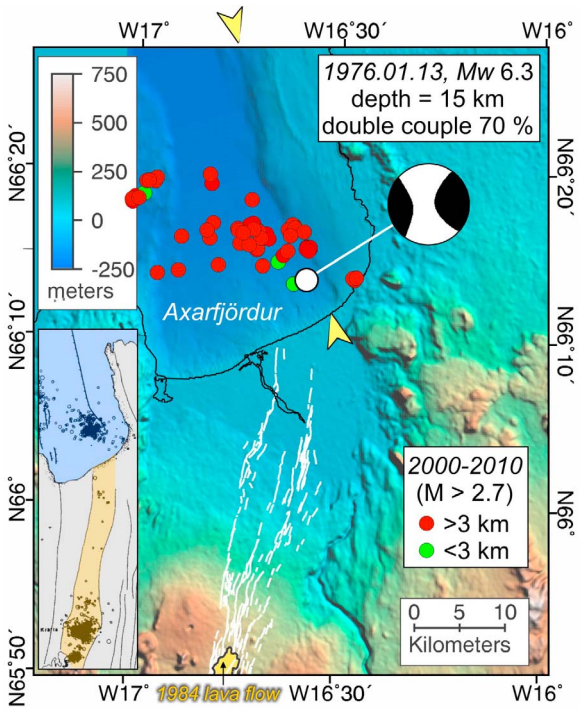

Figure 12. Bathymetry and topography of the northern Krafla fissure swarm. Faults are shown by white lines. The Engdahl catalog location for the 13th January 1976 earthquake is shown, along with the Harvard CMT solution. Red and green circles show microearthquakes at >3 km and <3 km depths, detected by the SIL network in the period 2000–2010. Inset figure shows microearthquakes recorded along the Krafla rift between 1981 and 1985 (adapted from *Einarsson*, [1991]). A major NNW-SSE striking normal fault scarp in the Axarfördur bay is highlighted by yellow pointers [*McMaster et al.*, 1977; *Einarsson*, 1991].

This weakening may be enough to activate faults which extend to the surface along the northern section of the rift. This effect could be enhanced if the northern rift is in a greater state of tension. Nevertheless, if the dike propagates so fast that the length of the pore pressure boundary layer is less than the rock grain size, which could be the case near the magma chamber, then the frictional resistance ahead of the dike tip fed by magmatic volatiles may also be reduced.

[38] Another explanation could be that the northern section opened at the surface in response to a deep dike injection sourced from the north, rather than the south; a relatively deep dike would be required to activate the normal faults bounding the 5 km wide rift. Dike injections sourced from different magma chambers along a rift zone was observed using satellite geodesy over the Afar rift in East Africa, which was activated during the 2005–2009 Afar rift crisis [*Wright et al.*, 2006; *Barisin et al.*, 2009; *Grandin et al.*, 2009]. In the early stages of the crisis, magma upwelling and dike injection in the Dabbahu-Gabho area at the northern end of the rift triggered further rifting and deep magma chamber discharge (10 km depth) in the Manda Hararo section of the rift 30 km to the south. Elastic dislocation modeling of geodetic data indicate significant variations in the magnitude of fault slip and dike opening along the rift zone, with a patch of low opening separating the Dabbahu-Gabho and Manda Hararo regions [*Wright et al.*, 2006; *Barisin et al.*, 2009; *Grandin et al.*, 2009] — the 5 km width of this low slip section is nevertheless much smaller than the 20 km section at Krafla. Injection of a dike at depth beneath the northern Krafla rift early in the crisis may explain some aspects of the seismicity resulting the Krafla rift crisis. These are discussed below.

5.3. Seismicity of the Early Krafla Rifting Crisis

[39] On the 13th January 1975, the largest earthquake (M_w 6.4) of the crisis occurred at the northern end of the rift, some 5 km north of the Axarfjördur coastline (Figure 12). The earthquake centroid moment tensor (Global CMT) indicates significant strike-slip deformation during this event. Because the epicenter was located at the northern end of the rift zone, and the event occurred just a few weeks after the initial dike injection, *Björnsson et al.* [1977] interpreted it as resulting from right-lateral slip on a NW-SE transform fault, the Grimsey Lineament, which was thought to form a structural termination to the rift zone, in response to loading caused by the earlier dike injection. However, bathymetric data from the Axarfjördur region does not reveal any geomorphic features typical of prolonged right-lateral strike-slip activity. Major NNW-SSE trending scarps are clearly visible in the bathymetry, typical of normal faults, suggesting that the Krafla rift zone continues northward beyond the location of the 1976 earthquake epicenter. *Rögnvaldsson et al.* [1998] concluded right-lateral shear across the Grimsey Lineament is actually accommodated by block rotation between N-S faults which strike perpendicular to the transform fault, i.e. there is no single throughgoing transform fault in this region.

[40] The relocated hypocenter for the 1976 event [*Engdahl et al.*, 1998] is located directly above one of these normal faults, which strikes NNW for >30 km along the eastern margin of Axarfjördur bay (shown by yellow pointers in Figure 12). The 1976 hypocenter also coincides with a patch of micro-earthquakes from the period 1981–1986 [*Einarsson*, 1991] and 2000–2010 (SIL catalog, see Figure 12). The depth distribution for these events indicates brittle behavior throughout the entire crust, with 80% occurring between 3–15 km depth [see also *Rögnvaldsson et al.*, 1998]. This cluster of activity closely resembles another cluster of earthquakes to the south, associated with magmatic intrusion beneath the Krafla caldera between 1981–1986 (Figure 12 inset). This similarity may indicate a similar response of the crust to the change in stresses associated with magma upwelling and dike injection.

[41] The 1976 earthquake focal mechanism also contains a significant (30%) non-double couple component. Similar focal mechanisms have been reported in the Long Valley Caldera [*Julian*, 1983], which were originally interpreted as oblique strike-slip earthquakes, before being re-interpreted as CLVD mechanisms with a dilatational component associated with injection of fluids into the crust. CLVD mechanisms have also been reported for micro-earthquakes in the Krafla post-rifting period [*Foulger et al.*, 1989]. (On the 12th December 1980 a similar CLVD mechanism also occurred ~60 km NW of the 1976 Krafla earthquake on the Grimsey Lineament, and may also be related to N-S injection of a dike at depth in 1980; Figure 1). Because the 1976 focal mechanism includes a significant dilatational component, the strike of a dike injected at depth would be approximately NNW-SSE, consistent with the strike of the normal faults at the surface (Figure 12) [see also

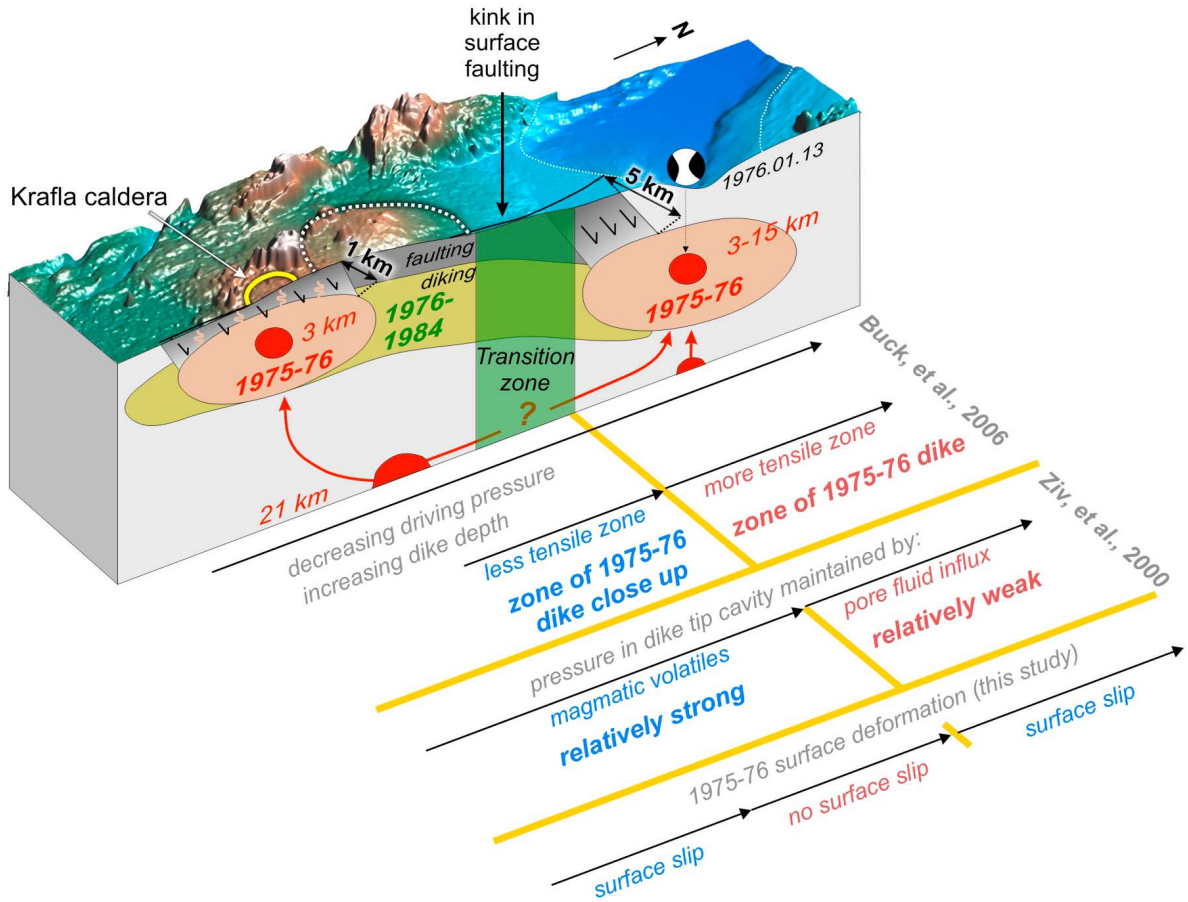

Figure 13. Schematic cross section along the Krafla rift zone summarizing the general sub-surface movements of magma throughout the 1975–1984 rift crisis. Thick dotted white line shows the Storaviti and Grjothals topographic high; yellow line shows the Krafla caldera; thin white dotted line shows the coastline. Red areas show possible magma chambers at depth; pink areas show significant dike opening during the early stages of the crisis; yellow regions show significant dike opening in the mid-to-late stages of the crisis; dark gray region shows the region above the dike, which failed by faulting. Various aspects from the studies of *Buck et al.* [2006] and *Ziv et al.* [2000] relating to dike propagation and strength of the crust, and which may explain the bi-modal pattern of surface opening (this study) are summarized alongside the figure, see Section 5.2 for details. Green section of the crust indicates the transition from magmatic volatiles to influx of pore fluids in the dike tip cavity. See Section 5.2 for additional discussion.

McMaster et al., 1977]. However, it should be noted that the non-double couple component could simply reflect a more complicated earthquake source, including multiple double-couple, or both dilatational and double-couple sub-events.

[42] Although the various dike injections of the Krafla rifting crisis may have been sourced from various magma sources, lateral dike injection has clearly played an important role in accommodating along-strike opening of the Krafla fissure swarm [e.g., *Einarsson and Brandsdottir*, 1980]. Therefore, perhaps the most likely scenario which explains both the seismicity, and pattern of surface opening is one in which a dike propagates from the caldera northward into a region of higher tension at the northern end of the rift [*Buck et al.*, 2006]. Surface faults are activated in the south as a result of wider opening on a shallower dike. Surface faulting in the north occurs above a thinner deeper dike because the host rock is weakened due to the transition from magmatic volatiles to ambient pore fluids feeding the dike tip cavity [*Ziv et al.*, 2000]. In this model, a relatively large and deep packet of magma would be delivered to the northern end of the Krafla rift, enough to activate normal faults at this location. Because the normal faults extend to greater depths in the crust, where they coincide with the dike top, they will have a bigger area than those closer to the caldera. Combined dike opening and normal slip on relatively large faults may therefore account for both the shear and dilatational components in the 1976 earthquake focal mechanism, as well as the epicentral location at the northern end of the rift Figure 12. These conclusions are summarized on a crustal profile along the Krafla rift, shown in Figure 13. It is also worth noting that *Einarsson and Brandsdottir* [1980] report a kink in the seismicity associated with the July 1978 dike injection, which propagated from the Krafla caldera to N66°3′ (Figure 4, and thick black arrow in Figure 13). This kink corresponds to the region of no surface faulting in the central rift at the start of the crisis, and may highlight a structural complexity at depth. The obliquity of the kink with respect to the strike of the wider Krafla rift raises the possibility that the January 1976

dike injection may have propagated through a self-generated crack analogous to 'wing-cracks' observed to form in the tips of pure mode-II fractures [*Ziv et al.*, 2000]. The generation of such a 'wing-crack' could occur at the transition of magmatic volatiles to ambient pore fluids feeding the dike tip cavity (Figure 13).

5.4. Implications for Magma Migration Throughout the Krafla Crust

[43] Although the shallow magma chamber beneath the Krafla caldera appears to have sourced material for the various dike injections throughout the crisis, *de Zeeuw-van Dalfsen et al.* [2004] detected a much deeper accumulation of magma using InSAR observations over the period 1993–99, which may have also contributed to deformation during the crisis. The location of this deep accumulation, ~15 km north of the Krafla caldera and at 21 km depth also coincides with the region of maximum opening during the 1975–1984 crisis, as well as two topographic highs (Storaviti and Grjothals), which make up a broader long-wavelength high across the center of the rift zone, similar to the Mando Hararo section of the Afar rift. Therefore, it is possible that the shallow magma chamber beneath the caldera may have been sourced from a deeper, more centrally located magma chamber (Figure 10a), which may also have sourced a magma chamber to the north (Figure 13). This idea is also consistent with geochemical data from the Krafla region [*Nicholson et al.*, 1991; *Gronvold*, 2006; *Maclennan et al.*, 2008], which shows significant variability in the depth of magma sources throughout the Krafla rift, particularly within and outside the caldera. However, it should be noted that the long-wavelength post-rifting signal over the Storaviti-Grjothals high may also be explained by visco-elastic relaxation models [e.g., *de Zeeuw-van Dalfsen et al.*, 2004; *DiCaprio*, 2010], which also account for the co-location of the maximum post-rifting signal with the region of maximum co-rifting opening. *de Zeeuw-van Dalfsen et al.* [2004] rule out the visco-elastic relaxation hypothesis because the expected post-rifting deformation from *Pollitz and Sacks* [1996] is only 15% of the total broad deformation seen in their interferograms. However, *DiCaprio* [2010] showed that alternative post-rifting, viscoelastic models can exhibit much larger deformation rates. Nevertheless, a contraction of ~0.5 m was measured across the Krafla caldera region between 1965–71 [*Wendt et al.*, 1985], which could also be explained by deflation of the deep magma source of *de Zeeuw-van Dalfsen et al.* [2004], with melt migrating to shallower depths prior to the crisis. Similar migration of melt between 6–24th July 2007 from depths of 17.5 km to 13.5 km and at dip angles of 50° have recently been reported near Askja caldera, 80 km south of Krafla [*White et al.*, 2011].

6. Conclusions

[44] Correlation of a declassified KH-9 spy satellite image with a SPOT5 satellite image reveals the regional deformation pattern between 1977–2002 (2.5 m average opening), while correlation of aerial photos between 1957–1990 provide local measurements of the total extension close to the rift zone (average 4.3 m opening). These results were obtained using the COSI-Corr software package, which allows declassified spy satellite and aerial photos to be correlated with subpixel precision. Development of a new 'Epipolar Map Projection' tool within COSI-Corr also allows displacements to be measured in the epipolar perpendicular plane, which contains no topographic residuals. Therefore, high resolution optical imagery from different sources may now be successfully correlated without an equivalent resolution DEM. Our results provide new insights into the deformation accommodated at the northern end of the Krafla rift zone, where earlier geodetic measurements were relatively sparse. Correlation of aerial photos from 1957–1976 reveal the magnitude and extent of opening during the early stages of the crisis. This study provides new constraints on the displacement field resulting from the 1975–1984 Krafla rifting crisis, NE Iceland. Extension at the surface is accommodated primarily by normal faults which bound the rift zone, while extension is accommodated at depth by dike injection. A bi-modal pattern of opening along the rift during this period could be produced by two different magma sources, located at the northern and southern ends of the rift zone. This is similar to observations from the Afar rift zone in East Africa, where extensive and precise geodetic measurements allow the determination of dike opening and fault slip throughout the rift zone. Alternatively, the bi-modal pattern of opening may also result from a weakening of the host rock along the northern end of the rift, as magmatic volatiles transition to ambient pore fluids feeding the dike tip cavity. Variations in the magnitude of opening along the Krafla rift zone require that either different sections of the rift zone are subject to dike injection events at different times, or the remaining deformation is accommodated elsewhere in the region, such as the neighboring Theistareykir and Fremri-Námar fissure swarms. Our results are significant as they provide new information on how past dike injection events accommodate long-term plate spreading. Furthermore, this study highlights the potential of optical image correlation using inexpensive declassified spy satellite and aerial photography to measure deformation of the Earth's surface going back many decades. This latter point highlights the potential of image correlation for providing important contributions in other areas of Earth surface observation, and for periods where InSAR and GPS data are not available, such as glacial studies, landsliding, coastal erosion, volcano monitoring as well as earthquake studies.

Appendix A: Optical Image Correlation Methodology

[45] Here we provide further details on the methodology used to correlate SPOT5 and KH-9 satellite images, and aerial photos. All processing was done using the COSI-Corr software package, which is a plugin for ENVI Exelis.

A1. Orthorectification and Correlation of SPOT5 and KH-9 Satellite Images

[46] During the orthorectification process, both the SPOT5 and KH-9 images are resampled to correct for the effect of topography, which occurs because of the stereoscopic effect produced when images are acquired with an oblique view of the Earth's surface (i.e. off-nadir incidence angles). Orthorectification gives both images a common viewing geometry, equivalent to the satellite looking exactly normal to Earth's surface everywhere across the image, after which

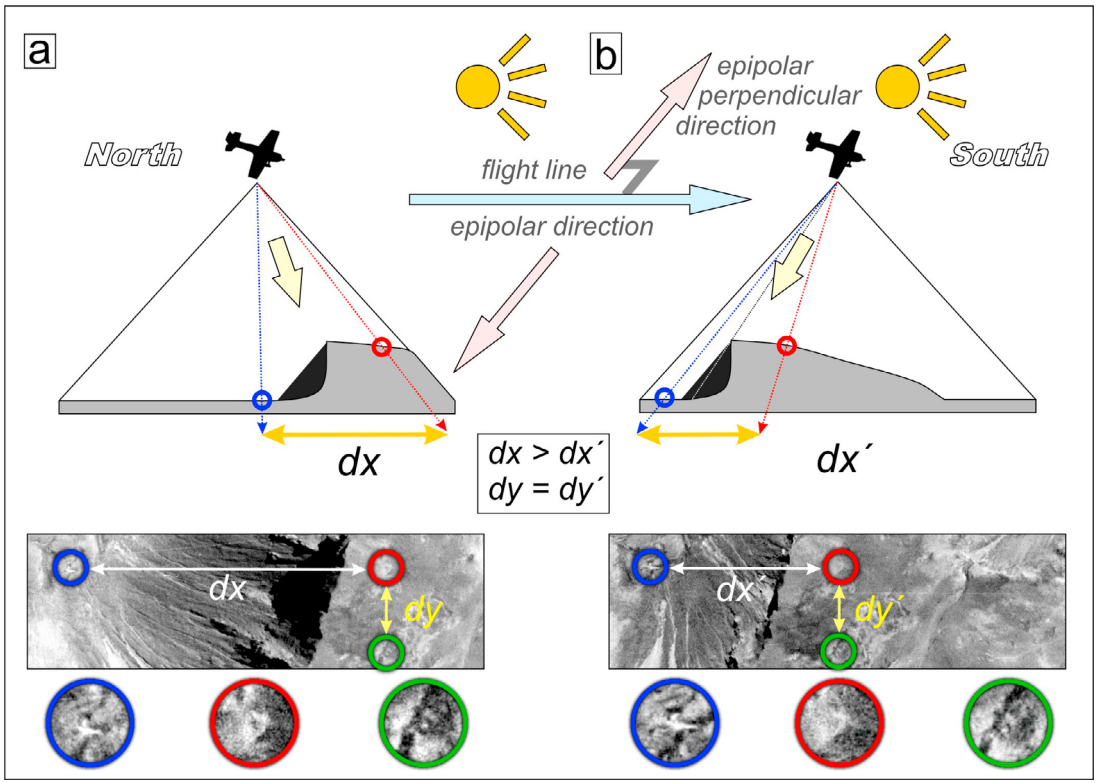

Figure A1. As an airplane flies over the ground (i.e. from point a to b) acquiring aerial photos, the incidence angle changes across the image. The result is that the ground is viewed at different oblique angles around the edges of the image, which result in visual differences of the same feature in the landscape (due to a change in parallax). The number of pixels (dx) between the red and blue features in Figure A1a, is much greater than the number of pixels (dx′) between the same features in Figure A1b, because the cliff which separates them is being viewed at different angles. However, the number of pixels between the red and green features is the same in both images. This is because the viewing angle is the same for both the red and green features in the y-direction. Therefore, the parallax difference between the images is greatest in one direction, known as the epipolar direction, and in this example corresponds to the flight direction of the airplane. Topographic information can be extracted from aerial photos reprojected into the epipolar plane. Conversely, there is no topographic information recorded in the epipolar perpendicular direction.

they can be correlated to measure horizontal tectonic displacements. If the two images are not corrected for topography, the offset or disparity map will include a tectonic displacement overprinted by a much larger topographic signal which results from the parallax difference between the two images (Figure A1). To precisely orthorectify SPOT5 and KH-9 images, a digital elevation model of a similar resolution to the image acquisitions, and ideally from the same time period is needed. Unfortunately, the limited availability of suitable topographic data precludes such a precise orthorectification. Therefore, we use the 30 m global ASTER GDEM, which is produced by stereo extraction and stacking of multiple ASTER DEM's. We filter the ASTER GDEM with a 3 × 3 low-pass and 3 × 3 median filter to reduce high frequency noise.

A2. Post Processing: Removal of Topographic Residuals

[47] Due to the much lower resolution of the ASTER GDEM (30 m) compared with the KH-9 (~8 m) and SPOT5 (2.5 m) images, we cannot account for all of the topographic signal during orthorectification. This results in a displacement signal which correlates with high-frequency topographic noise in our correlation maps (Figure A2), thus slightly obscuring the tectonic signal. Because the parallax difference between the two images, i.e. the topographic signal, is at a maximum in the plane of parallax (also called the epipolar plane, see Figure A1), the topographic noise can be isolated by looking only at the epipolar plane displacement field. Conversely, the displacement perpendicular to the epipolar plane contains no topographic information (R. Binet, personal communication, 2010). We project our E-W and N-S displacement field into the epipolar and epipolar perpendicular displacement fields using the 'Epipolar Map Projection' tool in COSI-Corr (Figure A3). This allows us to measure the opening accommodated across the rift between September 1977 and October 2002 (Figure 4). For the KH-9-SPOT5 image pair (Figure 3), the epipolar perpendicular direction is approximately parallel to the maximum opening direction (i.e., WNW-ESE; see Figure A3) —the variation in this direction across the wider Krafla region results from differences between the radial incidence angle of the KH-9 image and the constant near-vertical incidence angle (0.78°

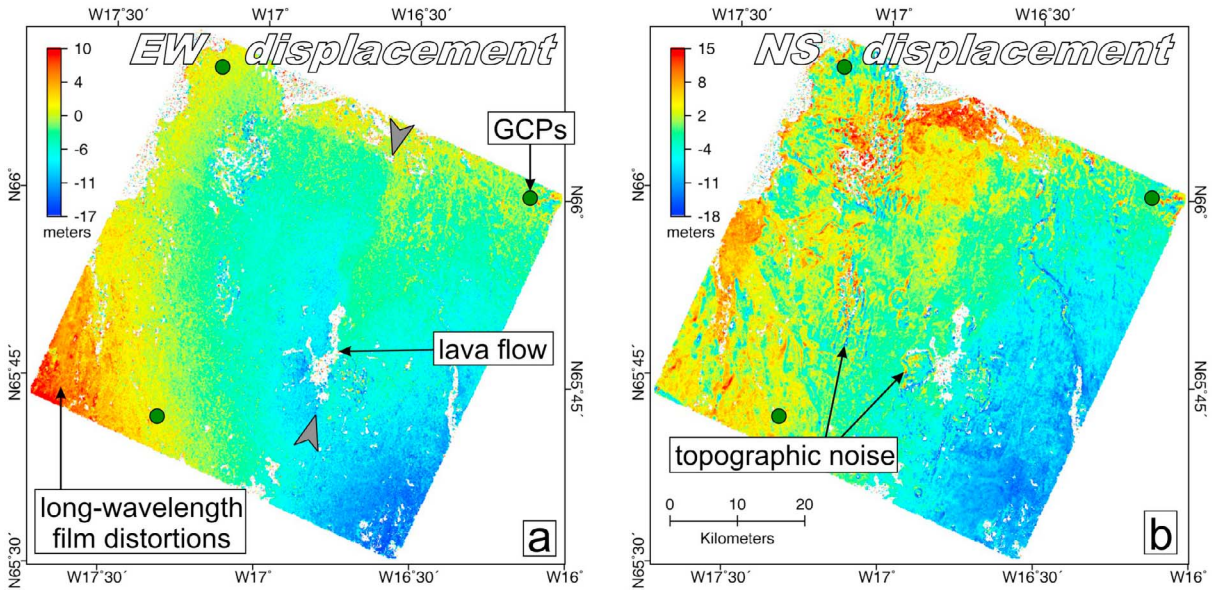

Figure A2. (a) East-west and (b) north-south displacement fields produced from correlation of the 1977 KH-9 and 2002 SPOT5 satellite images. The area covered by these images corresponds to that shown in Figures 3b and 3c. Positive values indicate eastward/northward movement of pixels between the two images. Opening of the Krafla rift zone occurred between the gray pointers in Figure A2a [see *Buck et al.*, 2006]. Eruption of lavas in 1984 results in a decorrelated patch around the caldera in both displacement maps. Green circles show the locations of tie points used to co-register the KH-9 image to the SPOT5 image.

east looking) angle of the SPOT5 image. However, the variation in epipolar direction across a 10 km wide zone over the Krafla fissure swarm is small (Figure A3a).

A3. Orthorectification and Correlation of Historical Aerial Photos

[48] Although KH-9 and traditional aerial photos may both be orthorectified using the 'Aerial Imagery' module

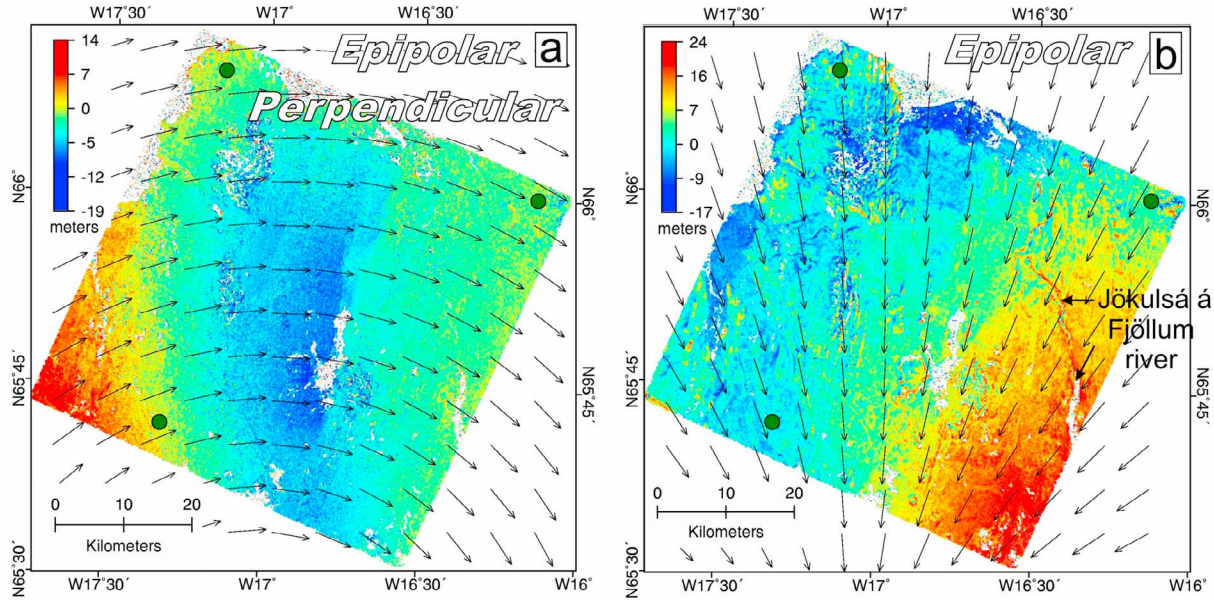

Figure A3. Reprojection of the KH-9-SPOT5 displacement maps into the (a) epipolar perpendicular, and (b) epipolar planes. Region corresponds to that shown in Figures 3b and 3c. Black arrows show the direction of these planes across the image, which vary due to combining a pushbroom satellite with a frame camera satellite system from different altitudes. Topographic noise, such as the Jökulsá á Fjöllum river valley, is visible in the epipolar direction, but not the epipolar perpendicular direction.

within COSI-Corr, a few important differences exist between KH-9 and aerial photos which may result in different correlation results. First, because camera calibration reports were supplied with the 1957 and 1990 aerial photos, we are able to generate more robust interior orientation models for the aerial camera systems used; this is not the case for the KH-9 images, for which the calibration reports remain classified. Therefore, using the aerial camera calibration information, we are able to account for optical distortions produced by the lens. Furthermore, a very precise and accurate determination of the focal length helps to reduce topographic residuals throughout the image, as well as enabling the photo to be successfully orthorectified.

[49] The high resolution of aerial photos (typically <1 m) means we need similarly high resolution digital elevation models to accurately orthorectify them. Unfortunately, the best available DEM we have for the Iceland region is the Global ASTER GDEM Version 1 (30 m). Orthorectifying aerial photos with such a coarse DEM means there are many topographic residuals remaining in the photos, which produce large displacement values during correlation, thus obscuring the real signal. Using high resolution stereo DEMs extracted from the aerial photos themselves does not account for all the topographic residuals, and may even add additional topographic noise if the two DEMs are not perfectly co-registered. We did not use pre- and post-crisis DEMs due to the significant challenges co-registering them precisely. We therefore orthorectify all aerial photos with the same ASTER GDEM, thereby providing consistency in processing between all data sets. We then reproject the displacement field into the epipolar and epipolar perpendicular geometry. Because the latter is free from stereoscopic effects, we analyze only epipolar perpendicular displacement fields for aerial photo correlations. It is therefore important to choose aerial photo pairs where the epipolar perpendicular directions are close to direction with the greatest displacement, i.e. rift-perpendicular for Krafla.

A4. Interpreting Vertical Deformations From Correlation of Aerial Photos and Satellite Images

[50] When the incidence angle for satellite images and aerial photos deviate from nadir, and the images become oblique to the Earth's surface, the images become increasingly sensitive to vertical deformation. This effect is particularly strong in aerial photos, where the incidence angle increases radially outwards from the center of the image, and therefore the sensitivity to topography increases around the edge of the photos. When we do not have adequate pre- and post-event DEMs, we must use the same DEM to orthorectify both the pre- and post-event aerial photos. However, any vertical displacement which occurs around the edges of the images will produce an apparent horizontal signal, because the same DEM was used for the pre- and post-event images (Figure A4) [*Copley et al.*, 2011].

[51] For the case where a camera is looking obliquely west at the ground, and there is subsidence between images, (Figure A4a) the subsidence will produce a positive eastward signal unless suitable pre- and post- DEM's are used to orthorectify the images. In the western parts of the image (Figure A4a), the camera is looking obliquely west. Therefore, if the green point in the post-crisis image has subsided from its original location, the blue circle in the pre-crisis image, which is orthorectified using the post-crisis DEM, will be projected to the location shown by the yellow circle. When correlating the pre- and post-crisis images, the yellow circle will appear to move eastward, thereby giving an apparent positive eastward displacement. If a camera is looking obliquely north (Figure A4b), a subsidence signal will produce an apparent southward displacement. In the northern part of an aerial photo, the camera looks obliquely north. Therefore, the green circle, which lies in the middle of the rift in the post-crisis, has subsided from its original position (blue circle), which then gets projected to the location of the yellow circle. Thus, the pre-crisis yellow circle appears to be displaced southward to the green circle location in the post-crisis image. If the incidence angle looks obliquely south or east, subsidence will produce a north or westward motion, respectively (Figure A4c). The resulting E-W displacement profile for a rift-zone oriented N-S is shown in Figures A4d–A4f. The eastern rift-flank is the stable reference area between the two images, and so the western-rift flank moves west, relative to the eastern rift-flank, thereby accommodating E-W extension. Subsidence and E-W extension are accommodated on N-S rift-bounding normal faults (14a). Subsidence occurs on the west side of the correlation/displacement map, and is therefore being imaged obliquely, looking west (Figures A4d and A4e). A profile of displacement taken across the rift is shown in Figure A4f. The eastern rift-flank is flat/stable, and both the inner rift and western rift-flank move to the west. However, the obliquity increases westward across the inner rift, which results in an increasing eastward component as one moves westward along the profile. If the heights of the east and western rift-flanks do not change considerably throughout the period of deformation, the E-W displacement of the western rift-flank will represent the total horizontal extension across the rift.

[52] Figure A5a shows how using the same post-crisis DEM can explain the positive eastward increase in displacement seen across the Northern Krafla inner rift (Figure 5). The pre-crisis topography is shown in green, and the post-crisis topography in gray; the black arrows show the camera incidence angles, which increase westward across the image. At the eastern rift boundary, shown by the heavy black line with fault arrows on the right of the image, the camera looks straight down. The blue circle represents a pixel in the post-crisis aerial photo, which moved from its original location in the pre-crisis topography, shown by the orange circle. When the pre-crisis aerial photo is orthorectified using the post-crisis DEM, the orange pixel is projected to the location shown by the red box. Image correlation measures the horizontal shift between the red and blue boxes. If there has been more normal slip on the eastern rift boundary than the western, consistent with our results, then the westward displacement measured by COSI-Corr will decrease westward. The thick black arrows along the bottom of the figure show the decrease in westward displacement across the image, which varies as a function of the camera incidence angle and elevation change. The percentage values are shown relative to the true westward displacement, δx, which is 100% and is constant everywhere west of the eastern rift boundary. Figure A5b shows the resulting E-W displacement profile (positive eastward

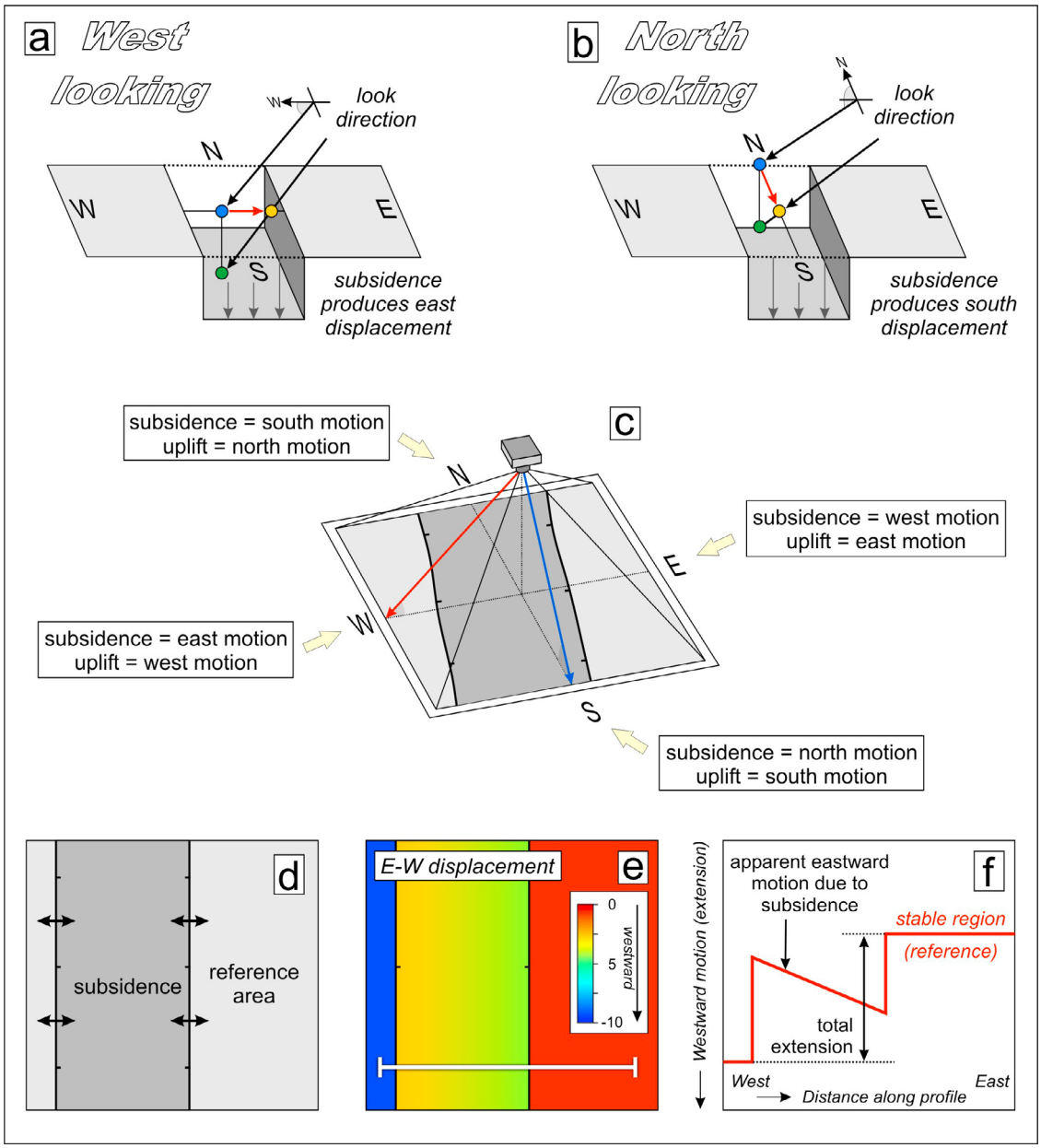

Figure A4. Cartoon showing the effect of using the same DEM for orthorectifying the pre- and post-crisis images, and changes in the camera viewing geometry on a displacement field involving vertical motions. If a camera is looking (a) obliquely west or (b) obliquely north, a subsidence signal will produce an apparent eastward and southward displacement, respectively (see text for details). (c) Summary diagram showing how vertical motions produce apparent horizontal displacements across different parts of an aerial photo. (d) Cartoon showing two rift bounding faults located at the western edge of an aerial photo correlation. Tie points are collected from the eastern rift flank; displacements are relative to this reference area. (e) The E-W displacement field resulting from normal slip on the two faults and (f) a profile of displacement is shown. Apparent eastward motion due to subsidence in the western part of the image produces a ramp in the inner rift displacement.

motion increases upwards). E-W extension is accommodated only on the eastern rift bounding fault, while both east and west bounding faults accommodate vertical motion, which produces the change in elevation between the two images. The resulting increase, or bulge in eastward displacement across the inner rift resembles the displacement profiles measured in the Northern Krafla Rift.

[53] In Figure A5a, the western rift flank has not changed elevation between the pre- and post-crisis images. However, leveling profiles across the northern Krafla rift which span the 1978 dike injection revealed significant rift flank uplift [*Sigurdsson*, 1980]. Figure A5c shows how rift flank uplift will affect the western Krafla rift boundary if a pre-crisis

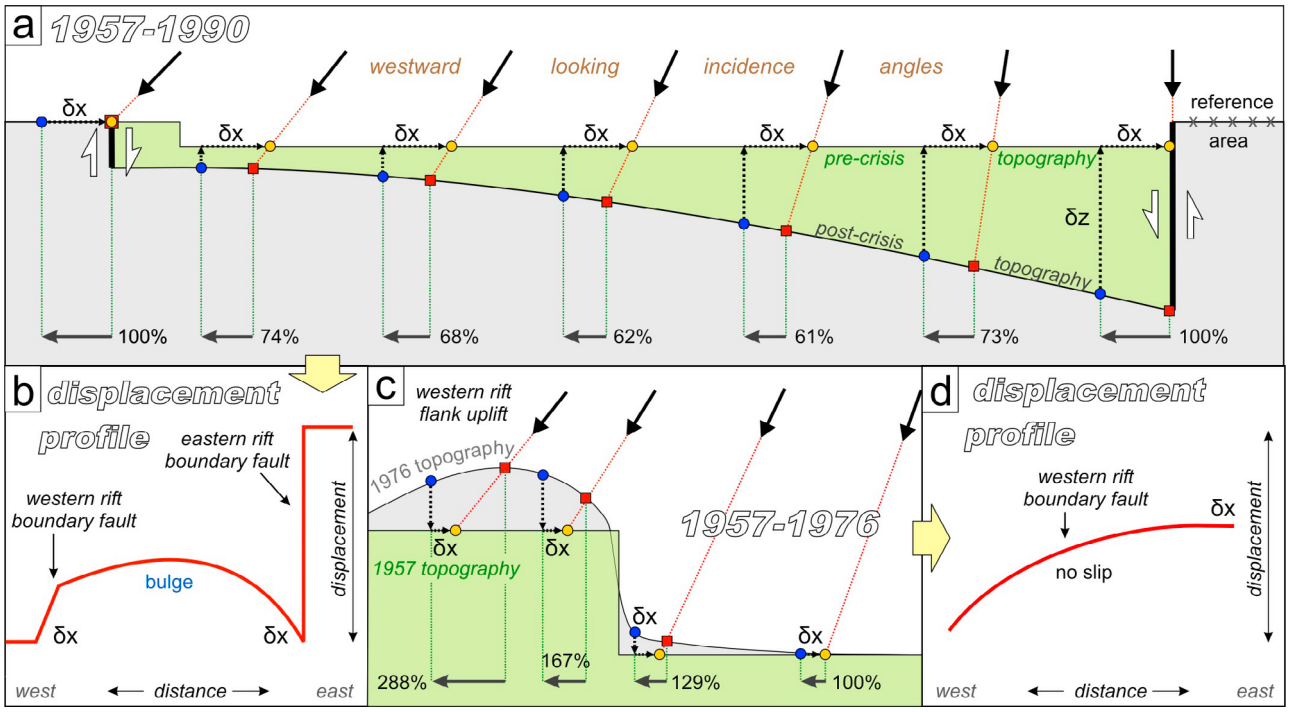

Figure A5. (a) Cartoon showing a profile across the Northern Krafla rift corresponding to the area imaged in the 1957–1990 aerial photo correlations (Figure 5). If the post-crisis DEM is used to orthorectify the pre-crisis aerial photos, post-crisis pixels (blue) are projected back to the locations shown by the red squares, which leads to an underestimation of the true westward displacement (δx) — see text for details. (b) Displacement profile across the rift shown in Figure A5a. Positive eastward displacement increases upwards. (c) Cartoon showing a profile across the western boundary of the Northern Krafla rift, corresponding to the area imaged in the 1957–1976 aerial photo correlations (Figure 8). If the 1976 topography is used to orthorectify the 1957 aerial photos, blue pixels in the 1976 image are projected back to the red squares, leading to an overestimation of the true westward displacement (δx) — see text for details. (d) Displacement profile across the rift shown in Figure A5c.

DEM is not used. Blue pixels in the post-crisis image move back to their original locations, orange circles, which are then projected back onto the post-crisis topography, red square locations. COSI-Corr will then measure the horizontal displacement between the blue circles and red squares, and will overestimate the real horizontal displacement where the pre-crisis topography was lower than the post-crisis topography. Figure A5d shows the resulting displacement profile, which increases exponentially toward the rift flanks. This effect may explain similar features seen at the edges of many of our correlations. For example, the large increase in westward motion seen in Figure 8 could occur if the 1976 dike injection did not activate the western boundary fault at this location. The resulting broad zone of uplift over the western rift flank would then produce an increase in the westward horizontal displacement value. This is a more likely explanation, because we do not see any distributed deformation outside of the rift zone in the KH-9-SPOT5 correlation (Figure 4).

[54] Finally, because all our aerial photos were acquired from flights paths oriented along the Krafla inner rift, the images always look westward at the western rift boundary and eastward at the eastern rift boundary. Because uplift occurs in the rift flanks, and subsidence in the inner rift, any vertical motion will produce an additional horizontal signal, rather than canceling out the real displacement (consistent with Figure A5c). Our estimates of extension are therefore likely to represent maximum values. Furthermore, this effect is specific to the geometry of the aerial photo survey and tectonic displacements at Krafla. Therefore, care must be taken when interpreting aerial photo displacement maps from other regions in which large vertical displacements have occurred.

[55] **Acknowledgments.** We thank the Gordon and Betty Moore Foundation and the Keck Institute for Space Studies for financial support. Arzan Surazakov provided helpful advice and discussion regarding orthorectification of KH-9 Hexagon data. The decision to look at displacement in the epipolar perpendicular direction was inspired by discussions with Renaud Binet. Bjarney Gudbjornsdottir and Carsten Kristinsson (National Land Survey of Iceland) were extremely helpful with locating and scanning all aerial photos used in this study. Tim Smith (USGS contractor working within Earth Resources Observation and Science, EROS Data Center) provided valuable assistance with scanning KH-9 spy satellite images. This work benefited from careful reviews by Amotz Agnon, and an anonymous reviewer. KH-9 data was obtained through the USGS EarthExplorer website. ASTER GDEM is a product of METI and NASA, and was obtained through the Reverb ECHO website. Níels Finsen of the Iceland Coast Guard kindly provided bathymetric data for the Axarfjördur region. Various aspects of this study benefited from discussions with Mark Simons, John Maclennan, Dan McKenzie, Gilles Peltzer, Sylvain Barbot, and Alex Copley. We are grateful to Heather Steele and Lisa Christiansen, who helped with ordering imagery and provided GIS support. All images in this study were processed using COSI-Corr, which is a plug-in for the ENVI software package. Various images in this paper were created using the ERDAS ERMapper software package, and the public domain Generic Mapping Tools (GMT) software [*Wessel and Smith*, 1998]. This is Tectonics Observatory contribution 210.

References

Abdallah, A., V. Courtillot, M. Kasser, A. Le Dain, J. Lépine, B. Robineau, J. Ruegg, P. Tapponnier, and A. Tarantola (1979), Relevance of Afar seismicity and volcanism to the mechanics of accreting plate boundaries, *Nature*, *282*, 17–23.

Agnon, A., and V. Lyakhovsky (1995), Damage distribution and localization during dyke intrusion, in *Physics and Chemistry of Dykes*, edited by H. Baer, pp. 65–78, A. A. Balkema, Rotterdam, Netherlands.

Árnadóttir, T., F. Sigmundsson, and P. Delaney (1998), Sources of crustal deformation associated with the Krafla, Iceland, eruption of September 1984, *Geophys. Res. Lett.*, *25*, 1043–1046.

Árnadóttir, T., B. Lund, W. Jiang, H. Geirsson, H. Björnsson, P. Einarsson, and T. Sigurdsson (2009), Glacial rebound and plate spreading: Results from the first countrywide GPS observations in Iceland, *Geophys. J. Int.*, *177*, 691–716, doi:10.1111/j.1365-246X.2008.04059.x.

Avouac, J.-P., F. Ayoub, S. Leprince, O. Konca, and D. Helmberger (2006), The 2005, Mw 7.6 Kashmir earthquake: Sub-pixel correlation of ASTER images and seismic waveforms analysis, *Earth Planet. Sci. Lett.*, *249*(3–4), 514–528.

Ayoub, F., S. Leprince, and J. Avouac (2009), Co-registration and correlation of aerial photographs for ground deformation measurements, *ISPRS J. Photogramm. Remote Sens.*, *64*(6), 551–560.

Baer, G., Y. Hamiel, G. Shamir, and R. Nof (2008), Evolution of a magma-driven earthquake swarm and triggering of the nearby Oldoinyo Lengai eruption, as resolved by InSAR, ground observations and elastic modeling, East African Rift, *Earth Planet. Sci. Lett.*, *272*, 339–352, doi:10.1016/j.epsl.2008.04.052.

Barisin, I., S. Leprince, B. Parsons, and T. Wright (2009), Surface displacements in the September 2005 Afar rifting event from satellite image matching: Asymmetric uplift and faulting, *Geophys. Res. Lett.*, *36*, L07301, doi:10.1029/2008GL036431.

Behn, M., W. Buck, and I. Sacks (2006), Topographic controls on dike injection in volcanic rift zones, *Earth Planet. Sci. Lett.*, *246*(3–4), 188–196, doi:10.1016/j.epsl.2006.04.005.

Biggs, J., F. Amelung, N. Gourmelen, T. Dixon, and S. Kim (2009), InSAR observations of 2007 Tanzania rifting episode reveal mixed fault and dyke extension in an immature continental rift, *Geophys. J. Int.*, *179*, 549–558, doi:10.1111/j.1365-246X.2009.04262.x.

Björnsson, A. (1985), Dynamics of crustal rifting in NE Iceland, *J Geophys. Res.*, *90*, 10,151–10,162.

Björnsson, A., K. Saemundsson, P. Einarsson, E. Tryggvason, and K. Gronvold (1977), Current rifting episode in North Iceland, *Nature*, *266*, 318–323.

Brandsdotttir, B., W. Menke, P. Einarsson, R. White, and R. Staples (1997), Faroe-Iceland ridge experiment: 2. Crustal structure of Krafia central volcano, *J Geophys. Res.*, *102*, 7867–7886.

Buck, W., P. Einarsson, and B. Brandsdóttir (2006), Tectonic stress and magma chamber size as controls on dike propagation: Constraints from the 1975–1984 Krafla rifting episode, *J. Geophys. Res.*, *111*, B12404, doi:10.1029/2005JB003879.

Calais, E., et al. (2008), Strain accommodation by slow slip and dyking in a youthful continental rift, East Africa, *Nature*, *456*, 783–787.

Cattin, R., C. Doubre, J. de Chabalier, G. King, C. Vigny, J. Avouac, and J. Ruegg (2005), Numerical modelling of quaternary deformation and post-rifting displacement in the Asal-Ghoubbet rift (Djibouti, Africa), *Earth Planet. Sci. Lett.*, *239*, 352–367.

Copley, A., J.-P. Avouac, J. Hollingsworth, and S. Leprince (2011), The 2001 Mw 7.6 Bhuj earthquake, low fault friction, and the crustal support of plate driving forces in India, *J. Geophys. Res.*, *116*, B08405, doi:10.1029/2010JB008137.

De Chabalier, J., and J. Avouac (1994), Kinematics of the Asal rift (Djibouti) determined from the deformation of Fieale volcano, *Science*, *265*, 1677–1681.

de Zeeuw-van Dalfsen, E., R. Pedersen, F. Sigmundsson, and C. Pagli (2004), Satellite radar interferometry 1993–1999 suggests deep accumulation of magma near the crust-mantle boundary at the Krafla volcanic system, Iceland, *Geophys. Res. Lett.*, *31*, L13611, doi:10.1029/2004GL020059.

DiCaprio, C. (2010), Measuring and modeling viscoelastic relaxation of the lithosphere with application to the northern volcanic zone, Iceland, PhD thesis, Calif. Inst. of Technol., Pasadena.

Einarsson, P. (1991), Earthquakes and present-day tectonism in Iceland, *Tectonophysics*, *189*, 261–279.

Einarsson, P., and B. Brandsdottir (1980), Seismological evidence for lateral magma intrusion during the July 1978 deflation of the Krafla volcano in NE-Iceland, *J. Geophys.*, *47*, 160–165.

Engdahl, E., R. van der Hilst, and R. Buland (1998), Global teleseismic earthquake relocation with improved travel times and procedures for depth determination, *Bull. Seismol. Soc. Am.*, *88*(3), 722–743.

Ewart, J., B. Voight, and A. Björnsson (1991), Elastic deformation models of Krafla Volcano, Iceland, for the decade 1975 through 1985, *Bull. Volcanol.*, *53*, 436–459.

Fialko, Y., and A. Rubin (1998), Thermodynamics of lateral dike propagation: Implications for crustal accretion at slow spreading midocean ridges, *J. Geophys. Res.*, *103*, 2501–2514.

Foulger, G., R. Long, P. Einarsson, and A. Bjornsson (1989), Implosive earthquakes at the active accretionary plate boundary in northern Iceland, *Nature*, *337*, 640–642.

Grandin, R., et al. (2009), September 2005 Manda Hararo-Dabbahu rifting event, Afar (Ethiopia): Constraints provided by geodetic data, *J. Geophys. Res.*, *114*, B08404, doi:10.1029/2008JB005843.

Grandin, R., A. Socquet, M.-P. Doin, E. Jacques, J.-B. de Chabalier, and G. King (2010a), Transient rift opening in response to multiple dike injections in the Manda Hararo rift (Afar, Ethiopia) imaged by time-dependent elastic inversion of interferometric synthetic aperture radar data, *J. Geophys. Res.*, *115*, B09403, doi:10.1029/2009JB006883.

Grandin, R., A. Socquet, E. Jacques, N. Mazzoni, J.-B. de Chabalier, and G. King (2010b), Sequence of rifting in Afar, Manda-Hararo rift, Ethiopia, 2005–2009: Time-space evolution and interactions between dikes from interferometric synthetic aperture radar and static stress change modeling, *J. Geophys. Res.*, *115*, B10413, doi:10.1029/2009JB000815.

Grandin, R., A. Socquet, C. Doubre, E. Jacques, and G. King (2012), Elastic thickness control of lateral dyke intrusion at mid-ocean ridges, *Earth Planet. Sci. Lett.*, *319–320*, 83–95.

Gronvold, K. (2006), Composition of Krafla Lavas 1975–84, *Eos Trans. AGU*, *87*(52), Fall Meet. Suppl., Abstract T33E-08.

Hauksson, E. (1983), Episodic rifting and volcanism at Krafla in North Iceland: Growth of large ground fissures along the plate boundary, *J. Geophys. Res.*, *88*, 626–636.

Jónasson, K. (1994), Rhyolite volcanism in the Krafla central volcano, north-east Iceland, *Bull. Volcanol.*, *56*(6–7), 516–528.

Julian, B. (1983), Evidence for dyke intrusion earthquake mechanisms near Long Valley caldera, California, *Nature*, *303*, 323–325.

Leprince, S., S. Barbot, F. Ayoub, and J.-P. Avouac (2007), Orthorectification, coregistration, and subpixel correlation of satellite images, application to ground deformation measurements, *IEEE Trans. Geosci. Remote Sens.*, *45*(6), 1529–1558.

Maclennan, J., E. Passmore, G. Fitton, T. Thordarson, and B. Winpenny (2008), Concurrent mixing and cooling of melts under Iceland, *J. Petrol.*, *49*, 1931–1953.

McMaster, R., J. Schilling, and P. Pinet (1977), Plate boundary within Tjörnes Fracture Zone on northern Iceland's insular margin, *Nature*, *269*, 663–668.

Michel, R., and J. Avouac (2002), Deformation due to the 17 August 1999 Izmit, Turkey, earthquake measured from SPOT images, *J. Geophys. Res.*, *107*(B4), 2062, doi:10.1029/2000JB000102.

Michel, R., and J. Avouac (2006), Coseismic surface deformation from air photos: The Kickapoo step over in the 1992 Landers rupture, *J. Geophys. Res.*, *111*, B03408, doi:10.1029/2005JB003776.

Mollberg, B., and B. Schardt (1988), Mission report on the Orbiter Camera Payload System (OCPS) Large Format Camera (LFC) and Attitude Reference System (ARS), *Tech. Rep. JSC-23184*, Johnson Space Cent., Houston, Tex.

Nicholson, H., M. Condomines, J. Fitton, A. Fallick, K. Gronvold, and G. Rogers (1991), Geochemical and isotopic evidence for crustal assimilation beneath Krafla, Iceland, *J. Petrol.*, *32*, 1005–1020.

Oskin, M., et al. (2012), Near-field deformation from the El Mayor-Cucapah earthquake revealed by differential LIDAR, *Science*, *335*, 702–705.

Pinzuti, P., A. Mignan, and G. King (2010), Surface morphology of active normal faults in hard rock: Implications for the mechanics of the Asal Rift, Djibouti, *Earth Planet. Sci. Lett.*, *299*, 169–179.

Pollitz, F., and I. Sacks (1996), Viscosity structure beneath northeast Iceland, *J. Geophys. Res.*, *101*, 17,771–17,793.

Rögnvaldsson, S., A. Gudmundsson, and R. Slunga (1998), Seismotectonic analysis of the Tjörnes Fracture Zone, an active transform fault in north Iceland, *J. Geophys. Res.*, *103*, 30,117–30,129.

Rubin, A. (1992), Dike-induced faulting and graben subsidence in volcanic rift zones, *J. Geophys. Res.*, *97*, 1839–1858.

Rubin, A., and D. Pollard (1988), Dike-induced faulting in rift zones of Iceland and Afar, *Geology*, *16*, 413–417.

Ruegg, J., and M. Kasser (1987), Deformation across the Asal-Ghobbet rift, Djibouti, Uplift and crustal extension, 1979–1986, *Geophys. Res. Lett.*, *14*, 745–748.

Sigmundsson, F. (2006), *Iceland Geodynamics: Crustal Deformation and Divergent Plate Tectonics*, Springer, New York.

Sigmundsson, F., et al. (2010), Intrusion triggering of the 2010 Eyjafjallajökull explosive eruption, *Nature*, *468*, 423–430, doi:10.1038/nature09558.

Sigurdsson, O. (1980), Surface deformation of the Krafla fissure swarm in two rifting events, *J. Geophys.*, *47*, 154–159.

Surazakov, A., and V. Aizen (2010), Positional accuracy evaluation of declassified Hexagon KH-9 mapping camera imagery, *Photogramm. Eng. Remote Sens.*, *76*, 603–608.

Tryggvason, E. (1976), Ground movement in North Iceland during the earthquake swarm of 1975–1976 (in Icelandic, with English summary), *Náttúrufraedingurinn.*, *46*, 124–128.

Tryggvason, E. (1984), Widening of the Krafla fissure swarm during the 1975–1981 volcano-tectonic episode, *Bull. Volcanol.*, *47*(1), 47–69.

Tryggvason, E. (1994), Surface deformation at the Krafla volcano, North Iceland, 1982–1992, *Bull. Volcanol.*, *2*, 98–107, doi:10.1007/BF00304105.

Wei, S., et al. (2011), Superficial simplicity of the 2010 El Mayor-Cucapah earthquake of Baja California in Mexico, *Nat. Geosci.*, *4*, 615–618, doi:10.1038/ngeo1213.

Wendt, K., D. Möller, and B. Ritter (1985), Geodetic measurements of surface deformations during the present rifting episode in NE Iceland, *J. Geophys. Res.*, *90*, 10,163–10,172.

Wessel, P., and W. H. F. Smith (1998), New, improved version of Generic Mapping Tools released, *Eos Trans. AGU*, *79*(47), 579, doi:10.1029/98EO00426.

White, R., J. Drew, H. Martens, J. Key, H. Soosalu, and S. Jakobsdottir (2011), Dynamics of dyke intrusion in the mid-crust of Iceland, *Earth Planet. Sci. Lett.*, *304*(3–4), 300–312.

Wright, T., C. Ebinger, J. Biggs, A. Ayele, G. Yirgu, D. Keir, and A. Stork (2006), Magma-maintained rift segmentation at continental rupture in the 2005 Afar dyking episode, *Nature*, *442*, 291–294.

Ziv, A., A. Rubin, and A. Amotz (2000), Stability of dike intrusion along preexisting fractures, *J. Geophys. Res.*, *105*, 5947–5961.